

Performance Analysis of RIS-Aided Double Spatial Scattering Modulation for mmWave MIMO Systems

Xusheng Zhu, Wen Chen, *Senior Member, IEEE*, Qingqing Wu, *Senior Member, IEEE*,
Jun Li, *Senior Member, IEEE*, Nan Cheng, *Member, IEEE*, Fangjiong Chen, *Member, IEEE*,
and Changle Li, *Senior Member, IEEE*

Abstract—In this paper, we investigate a practical structure of reconfigurable intelligent surface (RIS)-based double spatial scattering modulation (DSSM) for millimeter-wave (mmWave) multiple-input multiple-output (MIMO) systems. A suboptimal detector is proposed, in which the beam direction is first demodulated according to the received beam strength, and then the remaining information is demodulated by adopting the maximum likelihood algorithm. Based on the proposed suboptimal detector, we derive the conditional pairwise error probability expression. Further, the exact numerical integral and closed-form expressions of unconditional pairwise error probability (UPEP) are derived via two different approaches. To provide more insights, we derive the upper bound and asymptotic expressions of UPEP. In addition, the diversity gain of RIS-DSSM scheme was also given. Furthermore, the union upper bound of average bit error probability (ABEP) is obtained by combing the UPEP and the number of error bits. Simulation results are provided to validate the derived upper bound and asymptotic expressions of ABEP. We found an interesting phenomenon that the ABEP performance of the proposed system-based phase shift keying is better than that of the quadrature amplitude modulation. Additionally, the performance advantage of ABEP is more significant with the increase of the number of RIS elements.

Index Terms—Reconfigurable intelligent surface, dual spatial scattering modulation, millimeter-wave, multiple-input multiple-output, average bit error probability.

I. INTRODUCTION

In the past decade, numerous innovative wireless communication technologies have emerged to address the escalating demand for higher data rates and the rapid expansion of data services. For instance, massive multiple-input multiple-output (MIMO) systems enhance network throughput by serving multiple users simultaneously, and millimeter-wave (mmWave) communications utilize broader bandwidths to boost data rates over point-to-point links [1], [2]. Although these technologies have greatly improved the spectral efficiency of wireless communication, their inherent characteristics of high hardware

cost and increased power consumption pose a competitive disadvantage in the development of next-generation wireless networks.

Recently, reconfigurable intelligent surface (RIS) has emerged as a promising technology for the sixth-generation (6G) wireless system, owing to its ability to create a customizable propagation environment at a low hardware cost and power consumption [3]. Essentially, the RIS comprises a two-dimensional meta-surface consisting of numerous low-cost reflecting elements, which can individually reflect incoming signals with adjustable phase shifts [4]. It is worth noting that the phase shifts can be adjusted by employing inexpensive negative diodes or varactor diodes via the RIS controller, which can manipulate the electromagnetic waves, thus improving the signal quality of service and extending the network coverage [5]. Unlike conventional transmit/reflect-array antennas, the RIS can be conveniently deployed to facilitate data transmission without requiring any power-hungry transmit radio-frequency (RF) chains for signal reception and transmission, thus significantly cutting hardware costs and energy consumption [6]. Explicitly, the RIS technology is initially advocated in single-input single-output (SISO) systems, where the passive RIS can be employed to reflect the incoming signal [7]. Although the introduction of RIS can significantly reduce the average bit error rate (ABEP) of the system, the transmission throughput of the SISO-assisted RIS structure is limited in meeting the growing demand for high throughput in future wireless communications. To enhance the transmission throughput, MIMO-based RIS architectures have been investigated [8]. Specifically, the initial efforts focused on channel estimation and passive beamforming, where the RIS modifies the amplitude and phase of the incident signal. With an increased number of antennas, the transmission throughput of the MIMO-RIS technology can be greatly improved [9]. However, the augmented cost and the growing complexity of signal processing exacerbate the practical implementation. Accordingly, further design of simplified MIMO-RIS structures is needed.

Spatial modulation (SM) is a widely investigated technology, as evidenced by previous studies [10]–[13]. The information conveyed by SM consists of two components, the spatial domain and the symbol domain, thereby enhancing spectral efficiency. It is worth noting that SM enables a transmitter (Tx) to use only one radio frequency (RF) chain, which can be activated by selecting a specific transmit antenna for each time slot based on the input bits. Since only one transmit

(Corresponding author: Wen Chen).

X. Zhu, W. Chen, and Q. Wu are with the Department of Electronic Engineering, Shanghai Jiao Tong University, Shanghai 200240, China (e-mail: xushengzhu@sjtu.edu.cn; wenchen@sjtu.edu.cn; qingqingwu@sjtu.edu.cn).

J. Li is with the School of Electronic and Optical Engineering, Nanjing University of Science Technology, Nanjing 210094, China (e-mail: jun.li@njust.edu.cn).

N. Cheng and C. Li are with the School of Telecommunications Engineering, Xidian University, Xi'an 710071, China (e-mail: nancheng@xidian.edu.cn; clli@mail.xidian.edu.cn).

F. Chen is with the School of Electronic and Information Engineering, South China University of Technology, Guangzhou 510641, China (e-mail: eefjchen@scut.edu.cn).

TABLE I
NOTATIONS IN THIS PAPER

Notations	Definitions
$\ \cdot\ $	Euclidean norm of a complex-value vector
$ \cdot $	Absolute value operation
$(\cdot)^H$	Conjugate transpose operator
$(\cdot)^T$	Transpose operator
$\mathcal{CN}(\mu, \sigma^2)$	Circularly symmetric complex Gaussian (CSCG) distribution
$\mathcal{N}(\mu, \sigma^2)$	Real Gaussian distribution
$\mathbb{C}^{n \times m}$	The space of $n \times m$ complex-valued matrices
\sim	"Distributed as"
$\text{diag}(\cdot)$	Diagonal matrix operation
$\arg[\cdot]$	Phase operations on complex numbers
P_s	The average transmit power
$\delta(\cdot)$	Delta function
$\exp(\cdot)$	Exponential function
$\Pr(\cdot)$	Probability of the event occurring
$ \cdot $	The absolute value operation
P_b	CPEP
P_b	UPEP
$\Re\{\cdot\}$	Real part operation
$\Im\{\cdot\}$	Imaginary part operation
$E(\cdot)$	Expectation operation
$\Gamma(\cdot)$	Gamma function
$W_{\cdot, \cdot}(\cdot)$	Whittaker function
$K_0(\cdot)$	Zeroth order modified Bessel function of second kind
$K_1(\cdot)$	First order modified Bessel function of second kind
$I_0(\cdot)$	Zero-order modified Bessel function of the first kind
$Q(\cdot)$	Q-function
ψ	Digamma function
$\text{erfc}(\cdot)$	Complementary error function
$(\cdot)!$	Factorial operation

antenna is active at each time slot and all others are inactive, SM strikes a trade-off between energy efficiency and spectral efficiency [10]. To investigate the propagation characteristics of SM in the real-world environment, the authors of [11] performed large-scale measurements to extract the channel impulse responses in the lecture room and indoor corridor under the line-of-sight (LoS) and non-line-of-sight (NLoS) scenarios, respectively. For analysis of the spatial domain information performance of SM, the authors of [12] introduced the concept of space shift keying (SSK), in which the signal of the symbol domain is stripped out and relies only on the signal of the spatial domain to complete the transmission. In particular, the authors of [13] presented the quadrature SM (QSM) scheme to increase the spectral efficiency by extending the SM into in-phase and quadrature dimensions. All of the above work is based on activating antennas at different locations in space to achieve information transmission, however, such techniques are hardly applicable in the mmWave band. Since the high-frequency wavelength of mmWave is quite small, this results in higher path loss in the propagation of information. Accordingly, it is difficult to efficiently deliver the desired signal to the target Rx through a single antenna in the mmWave band with SM and variants of SM techniques. On the other hand, the scarcity of low-band spectral resources, mmWave has a much wider band range, which effectively alleviates the spectral resource constraint. In view of this, spatial scattering modulation (SSM) scheme is proposed in [14], where the transmit beam of the SSM scheme can be applied at each transmission time slot instead of a single antenna, thus guaranteeing the quality of the signal. In contrast

to conventional SM schemes, the SSM also employs a single RF chain. However, instead of activating a transmit antenna at each time slot, the SSM activates a scatterer in the channel. In [15], the quadrature SSM scheme was studied, where the real and imaginary parts of the transmit signal are transmitted using different transmit beams, thereby enhancing spectral efficiency.

A. Related Works

Driven by the enhanced coverage of RIS and the improved spectral efficiency features of SM, the combination of the two has the potential to be an energy-efficient communication solution [16]–[20]. For instance, the author of [16] firstly modeled an RIS-assisted SM scheme, in which the RIS-SM scheme can acquire maximum signal-to-noise ratio (SNR) by adjusting the phase shifts of the RIS. Different from [16] only focused on the receive SM, the authors of [17] studied the large intelligent surface-assisted SM (LIS-SM) scheme by adopting SM both at the Tx and receiver (Rx). Besides, optimization problems aimed at minimizing the symbol error rate were respectively investigated under the transmitting SM and receiving SM scenarios [18]. In [19], Wu *et. al* concentrated on the modulation scheme for RIS-assisted symbiotic radio systems, where the primary and additional internet-of-things signals are jointly detected at the Rx. Additionally, the authors of [20] studied an energy-efficient architecture that leverages SM technology and RIS-assisted ambient backscatter (ABSc) communication. This architecture employs ABSc to capture energy from ambient RF waves, reducing power consumption and extending the battery life of wireless devices. Furthermore, [21] proposed a novel

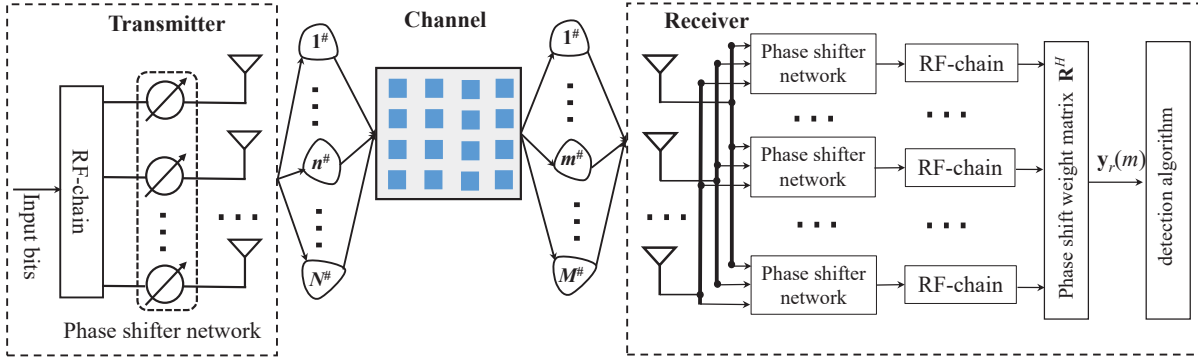


Fig. 1. System model of the proposed RIS-DSSM scheme.

reflection modulation scheme named RIS-assisted quadrature reflection modulation (RIS-QRM), which is used for simultaneous passive beamforming and information transmission. In particular, the works on RIS-assisted SSK schemes were investigated in [22]–[27]. For example, the performance of ABEP on RIS-SSK schemes was studied in [22]–[24]. To further improve the spectral efficiency, the authors of [25] derived the closed-form expression of ABEP and presented an RIS-SSK scheme with Alamouti space-time block coding. Unlike [25], the authors of [26] investigated the RIS-assisted receive quadrature space shift keying (RIS-RQSSK) scheme that increases the spectral efficiency by employing the real and imaginary dimensions independently. To improve the spectral efficiency of the RIS-SSK system, the RIS-assisted full-duplex SSK scheme was studied in [27], [28].

B. Motivation and Contribution

In this paper, we consider a point-to-point RIS-aided modulation for mmWave systems with large-scale antenna arrays at the Tx and Rx sides. Due to unfavorable channel conditions, the direct link between Tx and Rx is blocked out. For this reason, we resort to RIS to assist the communication between Tx and Rx. To fully exploit the gain of RIS for modulation systems in the mmWave band, it is essential to investigate the RIS-assisted SSM system, which has potential applications in secure communication. Concretely, the code represented by the participating scatterers is known only to Tx and Rx. Meanwhile, it is very hard for an eavesdropper to recognize the code by the participating scatterers, especially in mobile communication scenarios where the scatterers are continuously changing.

Up to now, research on RIS-assisted SSM transmission has been still in its infancy. Fortunately, there are similar studies such as the work presented in [29]–[31]. To be specific, [29] and [30] considered a scenario in which the RIS is installed closer to the Tx and farther away from the Rx, where the Tx-RIS and RIS-Rx channels exchange information via line-of-sight (LoS) and non-LoS (NLoS) paths, respectively. Moreover, [31] investigated a more general RIS-double SSM (SSM) model, in which both Tx-RIS and RIS-Rx channels are communicated with the NLoS paths. In particular, [31] considered that the scatterer gains of the two sub-channels are arranged in descending order, which significantly increases the

complexity of deriving the probability density function (PDF) of the cascade channel, rendering the problem too complicated to address. With respect to performance analysis, [31] only provides conditional pairwise error probability (CPEP) expressions without further derivation of unconditional pairwise error probability (UPEP) expressions. Furthermore, due to the high complexity of maximum likelihood (ML) detectors, [31] does not provide a low-complexity detection algorithm. To this end, this paper proposes a novel detection and decoding algorithm to comprehensively evaluate the performance of RIS-assisted DSSM systems. The main contributions of this work can be summarized as follows:

- We provide a new analytical framework on the performance analysis of RIS-DSSM scheme. A suboptimal detection algorithm is proposed in this paper and we compare it with the ML detection algorithm in terms of complexity and reliability.
- Considering a practical model for the phase shift and amplitude response, we derive exact integral expressions for the ABEP. To get additional insights into the impact of system parameters, we derive the closed-form and asymptotic expressions for the ABEP. Additionally, the diversity gain of the proposed RIS-DSSM scheme is also provided.
- Simulation results are in agreement with the analytical ABEP based on the exact integral expression. Besides, we adopt the derived integral expression to validate the asymptotic expression for the RIS-DSSM scheme. Furthermore, the RIS-DSSM scheme has better ABEP performance compared to the conventional SSM scheme when the number of RIS elements is relatively large.

The remaining sections of this paper are structured as follows. In Section II, we introduce the system model and propose a low-complexity suboptimal detector for the RIS-DSSM scheme. In Section III, the exact integral and closed-form expressions of UPEP are derived. Based on this, the union upper bound of ABEP is provided. After that, Simulation and analytical results are presented and discussed in Section IV. Finally, Section V gives a summary of this paper. Note that the notations of this paper are summarized in Table I.

II. SYSTEM MODEL

In this paper, we consider a point-to-point mmWave MIMO system shown in Fig. 1, where the Rx and Tx are equipped with N_r and N_t element uniform linear arrays (ULAs), respectively. Meanwhile, the RIS is deployed to assist the data transmission from the Tx to the Rx, and RIS is composed of L reflecting elements. To characterize the limited scattering feature, we adopt the Saleh-Valenzuela (S-V) model to denote the sparse scattering of mmWave wireless propagation. There is a specific beam pointed to the candidate scatterer by phase shifter at each time slot. Since a single RF link is equipped at the Tx, only one transmitted beam can be generated to align the target scatterer. In other words, the transmit beam can only be aimed at the scatterers in the Tx-RIS channel or the scatterers in the Tx-Rx channel in each time slot. If the beam target the scatterer in the Tx-Rx channel, it becomes the conventional SSM schemes, which has been studied in [14]. In particular, if the RIS is far from the Tx or Rx, the effect of RIS assistance can be ignored. But this is not the consideration of this paper, since our goal is to investigate the performance of how much RIS can help SSM, where RIS is deployed not too far away from the Tx or Rx.

In this paper, we assume that Tx, Rx, and RIS can obtain perfect channel state information (CSI). However, in practical situations, channel estimation is unavoidable. Considering this, the RIS-DSSM scheme under ideal channel conditions can be taken as a limit for the actual channel estimation. When the channel estimation error is considered, the performance of the RIS-DSSM system inevitably deteriorates, and this part of the study can be left to the interested reader to expand on this foundation.

A. RIS-DSSM Transmission

In the RIS-DSSM scheme, the information stream consists of three parts, i.e., spatial beam stream in the Tx-RIS channel, spatial beam stream in the RIS-Rx channel, and symbol stream. Since the Tx employs a single RF chain, the beam is directed to a specific scatterer among the N scatterers at each time slot in the Tx-RIS channel. For the spatial domain signal stream in the RIS-Rx channel, the RIS controller can obtain perfect CSI of the Tx feedback so that the RIS can reflect the incident signal and be steered to a candidate scatterer among the M scatterers. Furthermore, the symbol domain signal adopts the K -ary phase shift keying/quadrature amplitude modulation (PSK/QAM). As a result, the total data rate for the proposed RIS-DSSM transmission can be represented as [15]

$$R = \log_2(N) + \log_2(M) + \log_2(K). \quad (1)$$

B. RIS-DSSM Channel Model

In Fig. 1, the RIS divides the channel into Tx-RIS channel and RIS-Rx channel. The channel matrix \mathbf{H} can be evaluated as

$$\mathbf{H} = \mathbf{H}_{\text{TI}} \Phi \mathbf{H}_{\text{RI}}, \quad (2)$$

where the phase-shifter matrix Φ at RIS can be expressed as

$$\Phi = \text{diag}(e^{j\phi_1}, \dots, e^{j\phi_L}) \in \mathbb{C}^{L \times L}, \quad (3)$$

where $\phi_l \in [0, 2\pi]$ represents the phase shift caused by the l -th RIS element to the incident signal, $\mathbf{H}_{\text{TI}} \in \mathbb{C}^{L \times N_t}$ and $\mathbf{H}_{\text{RI}} \in \mathbb{C}^{N_r \times L}$ denote channel matrix between the Tx and the RIS and between the RIS and Rx, respectively. In mmWave channels, a geometrical channel model is widely applied. Since the channel in mmWave systems has limited scattering, we can simplify the channel by assuming each cluster only contributes one path to the channel matrix [14]. Without loss of generality, we adopt the narrow band discrete physical channel model, which is an equivalent simplified version of the geometrical channel. Here, the \mathbf{H}_{TI} and \mathbf{H}_{RI} can be characterized as¹

$$\begin{aligned} \mathbf{H}_{\text{TI}} &= \sum_{n=1}^N g_n \alpha_r(\vartheta_n^r, \eta_n^r) \alpha_t^H(\theta_n^t), \\ \mathbf{H}_{\text{RI}} &= \sum_{m=1}^M h_m \mathbf{a}_r(\theta_m^r) \alpha_t^H(\vartheta_m^t, \eta_m^t), \end{aligned} \quad (4)$$

where N and M are the numbers of candidate scatterers in the Tx-RIS and RIS-Rx channels, respectively; g_n and h_m stand for the complex gains of the n -th and m -th scatterers in the Tx-RIS and RIS-Rx channels, respectively; $g_n \sim \mathcal{CN}(0, 1)$ and $h_m \sim \mathcal{CN}(0, 1)$ represent the complex gains of the n -th and m -th scatterers from the Tx-RIS and RIS-Rx channels, respectively. The steering vectors of the Rx and Tx with ULAs can be respectively calculated as

$$\begin{aligned} \mathbf{a}_r(\theta_m^r) &= \frac{1}{\sqrt{N_r}} [1, e^{j\frac{2\pi d_r}{\lambda} \sin(\theta_m^r)}, \dots, e^{j\frac{2\pi d_r}{\lambda} (N_r-1) \sin(\theta_m^r)}]^T, \\ \mathbf{a}_t(\theta_n^t) &= \frac{1}{\sqrt{N_t}} [1, e^{j\frac{2\pi d_t}{\lambda} \sin(\theta_n^t)}, \dots, e^{j\frac{2\pi d_t}{\lambda} (N_t-1) \sin(\theta_n^t)}]^T, \end{aligned} \quad (5)$$

where λ means the carrier wavelength. θ_m^r and θ_n^t stand for the angles of arrive and departure (AoA/AoD) for the m -th and n -th scatterers of channels \mathbf{H}_{RI} and \mathbf{H}_{TI} , respectively. Also, d_r and d_t denote the antenna spacings at the Rx and Tx sides, respectively. In addition, the RIS is a uniform planar array (UPA) with $L = L_h \times L_v$ reconfigurable passive components, where L_h and L_v represent the number of rows and columns of RIS, respectively. Here, the receive beam $\alpha_r(\vartheta^r, \eta^r)$ and transmit beam $\alpha_t(\vartheta^t, \eta^t)$ can be respectively characterized as

$$\begin{aligned} \alpha_r(\vartheta_n^r, \eta_n^r) &= [1, e^{j\frac{2\pi d}{\lambda} (\cos(\eta_n^r) \sin(\vartheta_n^r) + \sin(\eta_n^r))}, \dots, \\ &\quad e^{j\frac{2\pi d}{\lambda} ((L_h-1) \cos(\eta_n^r) \sin(\vartheta_n^r) + (L_v-1) \sin(\eta_n^r))}]^T, \\ \alpha_t(\vartheta_m^t, \eta_m^t) &= [1, e^{j\frac{2\pi d}{\lambda} (\cos(\eta_m^t) \sin(\vartheta_m^t) + \sin(\eta_m^t))}, \dots, \\ &\quad e^{j\frac{2\pi d}{\lambda} ((L_h-1) \cos(\eta_m^t) \sin(\vartheta_m^t) + (L_v-1) \sin(\eta_m^t))}]^T, \end{aligned} \quad (6)$$

where d denotes the interval of adjacent elements. ϑ^r and η^r are azimuth and elevation of AoA, respectively. Meanwhile, ϑ^t and η^t represent azimuth and elevation of AoD, respectively.

¹If there exist the LoS path between the Tx-RIS or RIS-Rx channels, the spatial domain modulation gain will disappear, and the spectral efficiency will decrease. In other words, if the transmitted beam and the reflected beam do not pass through the scatterers, the system degenerates into a traditional single-stream transmission communication system without SSM, and the spectral efficiency will be reduced.

Algorithm 1 Suboptimal Detector of the RIS-DSSM Scheme

```

1: Input:  $\mathbf{H}$ ,  $\mathbf{a}_r(\theta_m^r)$ ,  $\mathbf{a}_t^H(\theta_n^t)$ ,  $g_n$ ,  $h_m$ ,  $P_s$ ,  $n_r$ ,  $s_k$ ,  $M$ ,  $N$ ,  $K$ ,  $L$ 
2: Output: The detected  $h_{\hat{m}}$ ,  $g_{\hat{n}}$ ,  $s_{\hat{k}}$  for bit demapping.
3: for  $\hat{m} \leftarrow 1 : M$  do
4:   if  $\hat{m} == m$  then
5:      $\mathbf{y}_r(\hat{m}) \leftarrow \mathbf{a}_r^H(\theta_m^r) \mathbf{H} \mathbf{a}_t(\theta_n^t) \sqrt{P_s} s_k + n_r$ ;
6:   else
7:      $\mathbf{y}_r(\hat{m}) \leftarrow n_r$ ;
8:   end if
9: end for
10:  $\Delta_1 \leftarrow \infty$ ;
11: for  $m \leftarrow 1 : M$  do
12:   for  $n \leftarrow 1 : N$  do
13:     for  $k \leftarrow 1 : K$  do
14:        $r_1 \leftarrow \mathbf{a}_r^H(\theta_m^r) \mathbf{H} \mathbf{a}_t(\theta_n^t) \sqrt{P_s} s_k$ ;
15:        $\Delta_2 \leftarrow |\mathbf{y}_r(m) - r_1|$ ;
16:       if  $\Delta_2 < \Delta_1$  then
17:          $\hat{m} \leftarrow m$ ;    $\hat{n} \leftarrow n$ ;
18:          $\hat{k} \leftarrow k$ ;    $\Delta_1 \leftarrow \Delta_2$ ;
19:       end if
20:     end for
21:   end for
22: end for

```

Combing (3) and (4), the channel in (2) can be rewritten as

$$\mathbf{H} = \sum_{m=1}^M \sum_{l=1}^L \sum_{n=1}^N h_m g_n \mathbf{a}_r(\theta_m^r) \mathbf{a}_t^H(\vartheta_m^t, \eta_m^t) \times e^{j\phi_l} \mathbf{a}_r(\vartheta_n^r, \eta_n^r) \mathbf{a}_t^H(\theta_n^t). \quad (7)$$

Let us define $\zeta_m^t = \arg[\mathbf{a}_t(\vartheta_m^t, \eta_m^t)]$ and $\zeta_n^r = \arg[\mathbf{a}_r(\vartheta_n^r, \eta_n^r)]$. In this manner, (7) can be recast as

$$\mathbf{H} = \sum_{m=1}^M \sum_{l=1}^L \sum_{n=1}^N h_m g_n \mathbf{a}_r(\theta_m^r) e^{j(\phi_l + \zeta_m^t + \zeta_n^r)} \mathbf{a}_t^H(\theta_n^t). \quad (8)$$

Note that we consider a large number of transmit and receive array antennas equipped at the Tx and Rx. In this case, we use lemma 1 to give the corresponding characterization.

Lemma 1. *With a large number of antenna elements at both the Tx and Rx sides, we have*

$$\begin{aligned} \mathbf{a}_t^H(\theta_{l_1}) \mathbf{a}_t(\theta_{l_2}) &\approx \delta(l_1 - l_2), \\ \mathbf{a}_r^H(\theta_{l_1}) \mathbf{a}_r(\theta_{l_2}) &\approx \delta(l_1 - l_2). \end{aligned} \quad (9)$$

Proof: See Appendix A.

C. RIS-DSSM Detection

At the Rx, the received signal can be formulated as

$$\mathbf{y} = \sqrt{P_s} \mathbf{H} \mathbf{a}_t(\theta_n^t) s_k + \mathbf{n}, \quad (10)$$

Substituting (8) into (10), we have

$$\begin{aligned} \mathbf{y} &= \sqrt{P_s} \sum_{m=1}^M \sum_{l=1}^L \sum_{n=1}^N h_m g_n \mathbf{a}_r(\theta_m^r) e^{j(\phi_l + \zeta_m^t + \zeta_n^r)} \\ &\quad \times \mathbf{a}_t^H(\theta_n^t) \mathbf{a}_t(\theta_n^t) s_k + \mathbf{n}. \end{aligned} \quad (11)$$

Resort to lemma 1, (11) can be updated as

$$\mathbf{y} = \sqrt{P_s} \sum_{m=1}^M \sum_{l=1}^L h_m g_n \mathbf{a}_r(\theta_m^r) e^{j(\phi_l + \zeta_m^t + \zeta_n^r)} s_k + \mathbf{n}. \quad (12)$$

where \mathbf{n} stands for the noise vector following $\mathcal{CN}(0, N_0 \mathbf{I}_{N_r})$. It is assumed that Rx knows perfect CSI through channel estimation, each set of phase shifter networks connected to each RF chain is responsible for monitoring the beam from a specific scatterer. In Fig. 1, the received signal \mathbf{y} is filtered by M sets phase shifters. If the number of received RF chains is greater than M , Rx has the ability to distinguish the beam from a specific scatterer to achieve the correct decoding of spatial domain information. On the contrary, the number of RF chains is insufficient to detect the beam directions of all candidate scatterers, which will lead to a deterioration in the detected performance. Consequently, the weights of the minimum phase shifter network at Rx can be characterized as

$$\mathbf{R} = [\mathbf{a}_r(\theta_1^r), \dots, \mathbf{a}_r(\theta_m^r), \dots, \mathbf{a}_r(\theta_M^r)]. \quad (13)$$

After the RF chains, the received signal can be rewritten as

$$\mathbf{y}_r = \mathbf{R}^H \mathbf{y}. \quad (14)$$

Based on (12), the (14) can be further given as

$$\begin{aligned} \mathbf{y}_r &= \sqrt{P_s} \sum_{m=1}^M \sum_{l=1}^L h_m g_n \mathbf{a}_r^H(\theta_m^r) \mathbf{a}_r(\theta_m^r) \\ &\quad \times e^{j(\phi_l + \zeta_m^t + \zeta_n^r)} s_k + \mathbf{R}^H \mathbf{n}. \end{aligned} \quad (15)$$

By utilizing lemma 1, we have

$$\mathbf{y}_r = \sqrt{P_s} \sum_{l=1}^L h_m g_n e^{j(\phi_l + \zeta_m^t + \zeta_n^r)} s_k + \mathbf{R}^H \mathbf{n}. \quad (16)$$

The goal of RIS is to offset the transmit and receive beam by adjusting the phase shift, which can be set as $\phi_l + \zeta_m^t + \zeta_n^r = 0$. As such, we have

$$\mathbf{y}_r = \sqrt{P_s} L h_m g_n s_k + \mathbf{R}^H \mathbf{n}. \quad (17)$$

1) *Optimal Detector:* The ML detection algorithm of the proposed RIS-DSSM scheme can be formulated as

$$[\hat{n}, \hat{m}, \hat{k}] = \arg \min_{\substack{n \in \{1, \dots, N\} \\ m \in \{1, \dots, M\} \\ k \in \{1, \dots, K\}}} \left\| \mathbf{y}_r - \mathbf{a}_r^H(\theta_m^r) \mathbf{H} \mathbf{a}_t(\theta_n^t) \sqrt{P_s} s_k \right\|^2, \quad (18)$$

where \hat{n} , \hat{m} , \hat{k} stand for the indices of detected scatterers and symbol.

2) *Suboptimal Detector:* Since ML detection requires traversing all possibilities, this leads to the excessive complexity of decoding detection. To address this issue, we present a suboptimal detection algorithm. To be specific, we perform energy-based detection of the receiving beam index as

$$\hat{m} = \arg \max_{m \in \{1, 2, \dots, M\}} |\mathbf{y}_r(m)|^2, \quad (19)$$

where the receiving beam from \hat{m} -th scatterer with the maximum power is selected. Here, the signal at the \hat{m} -th RF chain can be characterized as

$$\begin{aligned} \mathbf{y}_r(\hat{m}) &= \mathbf{a}_r^H(\theta_{\hat{m}}^r) \mathbf{y} \\ &= \begin{cases} \mathbf{a}_r^H(\theta_{\hat{m}}^r) \mathbf{n}, & \hat{m} \neq m, \\ \mathbf{a}_r^H(\theta_m^r) \mathbf{H} \mathbf{a}_t(\theta_n^t) \sqrt{P_s} s_k + \mathbf{a}_r^H(\theta_m^r) \mathbf{n}, & \hat{m} = m. \end{cases} \end{aligned} \quad (20)$$

Assuming the scatterer decision in the RIS-Rx channel is correct, the signal from the m -th scatterer can be expressed as

$$\mathbf{y}_r(m) = \mathbf{a}_r^H(\theta_m^r) \mathbf{H} \mathbf{a}_t(\theta_n^t) \sqrt{P_s s_k} + n_r, \quad (21)$$

where noise term $n_r = \mathbf{a}_r^H(\theta_m^r) \mathbf{n}$ follows $\mathcal{CN}(0, N_0)$. Accordingly, the transmit signals can be jointly detected as

$$[\hat{n}, \hat{m}, \hat{k}] = \arg \min_{\substack{n \in \{1, \dots, N\} \\ m \in \{1, \dots, M\} \\ k \in \{1, \dots, K\}}} \left| \mathbf{y}_r(m) - \mathbf{a}_r^H(\theta_m^r) \mathbf{H} \mathbf{a}_t(\theta_n^t) \sqrt{P_s s_k} \right|^2. \quad (22)$$

III. PERFORMANCE ANALYSIS

Based on suboptimal detector provided in (22), the CPEP of the proposed RIS-DSSM can be calculated as

$$P_b = \Pr \left(\left| \mathbf{y}_r(m) - \mathbf{a}_r^H(\theta_m^r) \mathbf{H} \mathbf{a}_t(\theta_n^t) \sqrt{P_s s_k} \right|^2 > \left| \mathbf{y}_r(\hat{m}) - \mathbf{a}_r^H(\theta_{\hat{m}}^r) \mathbf{H} \mathbf{a}_t(\theta_{\hat{n}}^t) \sqrt{P_s s_{\hat{k}}} \right|^2 \right). \quad (23)$$

For subsequent analysis, we treat both sides of the inequality sign in (23) according to (19)-(22) to obtain

$$\left| \mathbf{y}_r(m) - \mathbf{a}_r^H(\theta_m^r) \mathbf{H} \mathbf{a}_t(\theta_n^t) \sqrt{P_s s_k} \right|^2 = |n_r|^2 \quad (24)$$

and

$$\left| \mathbf{y}_r(\hat{m}) - \mathbf{a}_r^H(\theta_{\hat{m}}^r) \mathbf{H} \mathbf{a}_t(\theta_{\hat{n}}^t) \sqrt{P_s s_{\hat{k}}} \right|^2 = \begin{cases} |n_r - \sqrt{P_s} L h_m g_n s_k - g_{\hat{n}} s_{\hat{k}}|^2, & \hat{m} \neq m \\ \left| \sqrt{P_s} L h_m (g_n s_k - g_{\hat{n}} s_{\hat{k}}) + n_r \right|^2, & \hat{m} = m. \end{cases} \quad (25)$$

After that, we will discuss the CPEP into two cases $\hat{m} = m$ and $\hat{m} \neq m$ separately.

A. $\hat{m} = m$

In this case, the beam decision at the RIS-Rx channel is correct, the CPEP can be derived by substituting (24) and (25) into (23) as

$$\begin{aligned} P_b &= \Pr \left(|n_r|^2 > \left| \sqrt{P_s} L h_m (g_n s_k - g_{\hat{n}} s_{\hat{k}}) + n_r \right|^2 \right) \\ &= \Pr \left(-2\Re \{ N_0 \sqrt{P_s} L h_m (g_n s_k - g_{\hat{n}} s_{\hat{k}}) \} \right. \\ &\quad \left. > \left| \sqrt{P_s} L h_m (g_n s_k - g_{\hat{n}} s_{\hat{k}}) \right|^2 \right) \\ &= \Pr \left(-2\Re \{ N_0 \sqrt{P_s} L h_m (g_n s_k - g_{\hat{n}} s_{\hat{k}}) \} \right. \\ &\quad \left. - \left| \sqrt{P_s} L h_m (g_n s_k - g_{\hat{n}} s_{\hat{k}}) \right|^2 > 0 \right) \\ &= \Pr (J > 0), \end{aligned} \quad (26)$$

where J follows $\mathcal{N}(\mu_J, \sigma_J^2)$, where the expectation and variance of J are $\mu_J = -\left| \sqrt{P_s} L h_m (g_n s_k - g_{\hat{n}} s_{\hat{k}}) \right|^2$ and $\sigma_J^2 = 2N_0 \sqrt{P_s} L h_m (g_n s_k - g_{\hat{n}} s_{\hat{k}})$, respectively. As such, the (26) can be further characterized as

$$P_b = Q \left(\sqrt{\frac{\mu_J^2}{\sigma_J^2}} \right) = Q \left(\sqrt{\frac{P_s |L h_m (g_n s_k - g_{\hat{n}} s_{\hat{k}})|^2}{2N_0}} \right). \quad (27)$$

Since g_n and s_k are coupled with each other, it is difficult to solve them directly. Consequently, we address this term by using **Lemma 2** as follows:

Lemma 2. To tackle this issue, let us define $\eta = |g_n s_k - g_{\hat{n}} s_{\hat{k}}|^2$, the average η can be characterized as

$$\bar{\eta} = \begin{cases} |s_k - s_{\hat{k}}|^2, & \hat{n} = n \\ |s_k|^2 + |s_{\hat{k}}|^2, & \hat{n} \neq n. \end{cases} \quad (28)$$

Proof: See in Appendix B. \blacksquare

To obtain the closed-form expression of the CPEP, we need to perform an expectation operation on channel variables, which can be expressed as

$$\bar{P}_b = \int_0^\infty Q \left(\sqrt{\frac{\rho L^2 \bar{\eta} x}{2}} \right) f(x) dx, \quad (29)$$

where $x = |g_n h_m|^2$, and $\rho = P_s/N_0$ denotes the average SNR. Then, we rely on the following theorem to obtain the PDF of the variable x .

Theorem 1. The PDF of $x = |g_n h_m|^2$ can be evaluated as $f(x) = 2K_0(2\sqrt{x})$. \blacksquare

Proof: See in Appendix C. \blacksquare

On the basis of **Theorem 1**, we substitute this into the (29). As such, the (29) can be formulated as

$$\bar{P}_b = 2 \int_0^\infty Q \left(\sqrt{\frac{\rho L^2 \bar{\eta} x}{2}} \right) K_0(2\sqrt{x}) dx. \quad (31)$$

In the following, we derive the PEP expression of the proposed RIS-DSSM scheme via the two methods.

1) **Method 1:** In this case, we derive the exact analytical expression of PEP depending on the numerical integral approach. To be specific, we substitute $Q(x) = \frac{1}{\pi} \int_0^\infty \exp\left(-\frac{x^2}{2\sin^2\theta}\right) d\theta$ into (31), the (31) can be rewritten as

$$\bar{P}_b = \frac{2}{\pi} \int_0^\infty \int_0^{\frac{\pi}{2}} \exp\left(-\frac{\rho L^2 \bar{\eta} x}{4\sin^2\theta}\right) K_0(2\sqrt{x}) d\theta dx. \quad (32)$$

By exchanging the order of integral variables θ and x , (32) can be recast as

$$\bar{P}_b = \frac{2}{\pi} \int_0^{\frac{\pi}{2}} \int_0^\infty \exp\left(-\frac{\rho L^2 \bar{\eta} x}{4\sin^2\theta}\right) K_0(2\sqrt{x}) dx d\theta. \quad (33)$$

To address the inner integral centrally, we let

$$\Lambda = \int_0^\infty \exp\left(-\frac{\rho L^2 \bar{\eta} x}{4\sin^2\theta}\right) K_0(2\sqrt{x}) dx. \quad (34)$$

Since the procedure for solving for (34) is tedious, we turn to [33]

$$\begin{aligned} &\int_0^\infty \exp(-\alpha x) K_{2\nu}(2\sqrt{\beta x}) dx \\ &= \frac{\exp\left(\frac{\beta}{2\alpha}\right)}{2\sqrt{\alpha\beta}} \Gamma(\nu+1) \Gamma(1-\nu) W_{-\frac{1}{2}, \nu} \left(\frac{\beta}{\alpha} \right). \end{aligned} \quad (35)$$

Afterwards, we substitute (35) into (34), the Λ can be expressed as

$$\begin{aligned} \Lambda &= \frac{\exp\left(\frac{2\sin^2\theta}{\rho L^2 \bar{\eta}}\right)}{\sqrt{\frac{\rho L^2 \bar{\eta}}{\sin^2\theta}}} \Gamma(1) \Gamma(1) W_{-\frac{1}{2}, 0} \left(\frac{4\sin^2\theta}{\rho L^2 \bar{\eta}} \right) \\ &= \frac{\exp\left(\frac{2\sin^2\theta}{\rho L^2 \bar{\eta}}\right) \sin\theta}{L\sqrt{\rho\bar{\eta}}} W_{-\frac{1}{2}, 0} \left(\frac{4\sin^2\theta}{\rho L^2 \bar{\eta}} \right). \end{aligned} \quad (36)$$

By combining (36) and (33), the UPEP can be obtained as

$$\begin{aligned}\bar{P}_b &= \frac{2}{\pi} \int_0^{\frac{\pi}{2}} \frac{\exp\left(\frac{2\sin^2\theta}{\rho L^2 \bar{\eta}}\right) \sin\theta}{L\sqrt{\rho\bar{\eta}}} W_{-\frac{1}{2},0}\left(\frac{4\sin^2\theta}{\rho L^2 \bar{\eta}}\right) d\theta \\ &= \frac{2}{\pi L\sqrt{\rho\bar{\eta}}} \int_0^{\frac{\pi}{2}} \exp\left(\frac{2\sin^2\theta}{\rho L^2 \bar{\eta}}\right) W_{-\frac{1}{2},0}\left(\frac{4\sin^2\theta}{\rho L^2 \bar{\eta}}\right) \sin\theta d\theta.\end{aligned}\quad (37)$$

Remark 1. Since (37) contains the Whittaker function, it does not satisfy the form of the closed-form expression. Recall that (37) is the integral variable $\theta \in [0, \frac{\pi}{2}]$, the upper bound in this case can be given as:

$$\bar{P}_b \leq \frac{2}{\pi L\sqrt{\rho\bar{\eta}}} \exp\left(\frac{2}{\rho L^2 \bar{\eta}}\right) W_{-\frac{1}{2},0}\left(\frac{4}{\rho L^2 \bar{\eta}}\right). \quad (38)$$

Although (38) satisfies the closure expression form, it is a loose upper bound of UPEP.

To obtain a more accurate UPEP closed-form expression, we provide an alternative method 2 to deal with it.

2) **Method 2:** In order to obtain the closed-form expression of (31), it is necessary to find an equivalent form of $K_0(x)$ function to expand it. Fortunately, according to [33], we can obtain

$$K_0(x) = -\ln\left(\frac{x}{2}\right) I_0(x) + \sum_{v=0}^{\infty} \frac{x^{2v}}{2^{2v}(v!)^2} \psi(v+1). \quad (39)$$

Further, the series expansion for the modified Bessel function $I_0(x)$ can be written as [33]

$$I_0(x) = \sum_{v=0}^{\infty} \frac{\left(\frac{x}{2}\right)^{2v}}{(v!)^2}. \quad (40)$$

Substituting (40) into (39), we have

$$K_0(x) = \sum_{v=0}^{\infty} \frac{x^{2v}}{2^{2v}(v!)^2} \left[-\ln\left(\frac{x}{2}\right) + \psi(v+1) \right]. \quad (41)$$

At this point, we substitute (41) into (31), then the detailed derivation of \bar{P}_b is given as follows:

$$\begin{aligned}\bar{P}_b &= 2 \int_0^{\infty} Q\left(\sqrt{\frac{\rho L^2 \bar{\eta} x}{2}}\right) \\ &\quad \times \left(\sum_{v=0}^{\infty} \frac{x^v}{(v!)^2} [-\ln(\sqrt{x}) + \psi(v+1)] \right) dx \\ &= 2 \sum_{k=0}^{\infty} \frac{1}{(k!)^2} \left[\int_0^{\infty} Q\left(\sqrt{\frac{\rho L^2 \bar{\eta} x}{2}}\right) \right. \\ &\quad \left. \times (x^k [\ln(\sqrt{x}) + \psi(k+1)]) dx \right] \\ &= -2 \sum_{v=0}^{\infty} \frac{1}{(v!)^2} \int_0^{\infty} Q\left(\sqrt{\frac{\rho L^2 \bar{\eta} x}{2}}\right) x^v \ln(\sqrt{x}) dx \\ &\quad + 2 \sum_{v=0}^{\infty} \frac{\psi(v+1)}{(v!)^2} \underbrace{\int_0^{\infty} Q\left(\sqrt{\frac{\rho L^2 \bar{\eta} x}{2}}\right) x^v dx}_{A_2} \\ &= - \sum_{v=0}^{\infty} \frac{1}{(v!)^2} \underbrace{\int_0^{\infty} Q\left(\sqrt{\frac{\rho L^2 \bar{\eta} x}{2}}\right) x^v \ln(x) dx}_{A_1} \\ &\quad + 2 \sum_{v=0}^{\infty} \frac{\psi(v+1)}{(v!)^2} A_2.\end{aligned}\quad (42)$$

Due to the complexity of the (42), it is challenging to solve it directly. In this case, we subsequently handle A_1 and A_2 in terms of **Theorem 2** and **Theorem 3**, respectively.

Theorem 2. The closed-form expression of A_1 can be given by

$$\begin{aligned}A_1 &= \frac{v!}{2} \left(\frac{4}{\rho L^2 \bar{\eta}}\right)^{v+1} \frac{(2v+1)!!}{(2v+2)!!} \\ &\quad \times \left[\ln\left(\frac{4}{\rho L^2 \bar{\eta}}\right) + \psi\left(v + \frac{3}{2}\right) - \frac{1}{v+1} \right].\end{aligned}\quad (43)$$

Proof: See in Appendix D. ■

Theorem 3. The closed-form expression for A_2 can be characterized as

$$A_2 = \frac{v!}{2} \left(\frac{4}{\rho L^2 \bar{\eta}}\right)^{v+1} \frac{(2v+1)!!}{(2v+2)!!}. \quad (44)$$

Proof: See in Appendix E. ■

By combing (43) and (44), the UPEP in (42) can be further calculated as

$$\begin{aligned}\bar{P}_b &= \sum_{v=0}^{\infty} \frac{2}{(v!)^2} \left[-\frac{1}{2} A_1 + \psi(v+1) A_2 \right] \\ &= \sum_{v=0}^{\infty} \frac{A_2}{(v!)^2} \left[-\ln\left(\frac{4}{\rho L^2 \bar{\eta}}\right) - \psi\left(v + \frac{3}{2}\right) \right. \\ &\quad \left. + \frac{1}{v+1} + 2\psi(v+1) \right] \\ &= \sum_{v=1}^{\infty} \frac{1}{2(v-1)!} \left(\frac{4}{\rho L^2 \bar{\eta}}\right)^v \frac{(2v-1)!!}{(2v)!!} \\ &\quad \times \left[-\ln\left(\frac{4}{\rho L^2 \bar{\eta}}\right) - \psi\left(v + \frac{1}{2}\right) + \frac{1}{v} + 2\psi(v) \right].\end{aligned}\quad (45)$$

B. $\hat{m} \neq m$

This situation indicates that the beam direction from RIS to Rx is incorrectly decided. Substituing (24) and (25) into (23), we have

$$P_b = P_r \left(|\mathbf{a}_r^H(\theta_m^r) \mathbf{n}|^2 > |\mathbf{a}_r^H(\theta_{\hat{m}}^r) \mathbf{n} - \sqrt{P_s} L h_{\hat{m}} g_{\hat{n}} s_{\hat{k}}|^2 \right). \quad (46)$$

Without loss of generality, let us define

$$w_1 = |\mathbf{a}_r^H(\theta_m^r) \mathbf{n}|^2, \quad w_2 = |\mathbf{a}_r^H(\theta_{\hat{m}}^r) \mathbf{n} - \sqrt{P_s} L h_{\hat{m}} g_{\hat{n}} s_{\hat{k}}|^2, \quad (47)$$

where $\mathbf{a}_r^H(\theta_m^r) \mathbf{n} \sim \mathcal{CN}(0, N_0)$ and $(\mathbf{a}_r^H(\theta_{\hat{m}}^r) \mathbf{n} - \sqrt{P_s} L h_{\hat{m}} g_{\hat{n}} s_{\hat{k}}) \sim \mathcal{CN}(-\sqrt{P_s} L h_{\hat{m}} g_{\hat{n}} s_{\hat{k}}, N_0)$. It can be easily found that w_1 is the central Chi-squared random variable with two degrees of freedom (DoFs), while w_2 means the non-central Chi-squared random variable with two DoF. Furthermore, let us make $x_1 = \frac{w_1}{N_0/2}$ and $x_2 = \frac{w_2}{N_0/2}$. At this moment, the central Chi-square distribution x_1 can be described as [32]

$$f_1(x_1) = \frac{1}{2} \exp\left(-\frac{x_1}{2}\right). \quad (48)$$

As a result, \bar{P}_b can be calculated as

$$\begin{aligned} P_b &= \frac{1}{2} \int_0^\infty f_2(x_2) \left(\int_{x_2}^\infty \exp\left(-\frac{x_1}{2}\right) dx_1 \right) dx_2 \\ &= \int_0^\infty f_2(x_2) \exp\left(-\frac{x_2}{2}\right) dx_2. \end{aligned} \quad (49)$$

It is observed that (49) satisfies the form of moment generating function (MGF). To address this issue, we resort to the solution provided by [32]. Accordingly, the MGF of noncentral Chi-square distribution with two DoFs can be evaluated as

$$M_s(x_2) = \left(\frac{1}{1 - 2s\sigma^2} \right) \exp\left(\frac{s\mu^2}{1 - 2s\sigma^2} \right). \quad (50)$$

Substituting (50) into (49), we get

$$P_b = \left(\frac{1}{1 + \sigma^2} \right) \exp\left(-\frac{\mu^2}{2(1 + \sigma^2)} \right). \quad (51)$$

For x_2 , we have $\sigma^2 = N_0$ and $\mu = -\sqrt{P_s} L h_{\hat{m}} g_{\hat{n}} s_{\hat{k}}$. Consequently, the CPEP can be calculated as

$$P_b = \frac{1}{2} \exp\left(-\frac{\rho L^2 |h_{\hat{m}} g_{\hat{n}}|^2 |s_{\hat{k}}|^2}{2} \right) = \frac{1}{2} \exp\left(-\frac{\rho L^2 |s_{\hat{k}}|^2}{2} x \right). \quad (52)$$

To eliminate the variables in (52) with respect to $h_{\hat{m}} g_{\hat{n}}$, we require an expectation operation into the CPEP-based derivation of the UPEP expression. In the following, the UPEP expressions in this context are derived by two methods.

1) **Method 1:** In this case, we derive the exact analytical expression of UPEP via numerical integration method.

Theorem 4. In this $\hat{m} \neq m$ case, the UPEP of RIS-DSSM scheme can be given by

$$\bar{P}_b = \frac{\exp\left(\frac{1}{2\alpha}\right)}{2\sqrt{\alpha}} W_{-\frac{1}{2}, 0} \left(\frac{1}{\alpha} \right), \quad (53)$$

where $\alpha = \frac{\rho L^2 |s_{\hat{k}}|^2}{2}$.

Proof: By combing (30) and (52), the UPEP can be calculated as

$$\bar{P}_b = \int_0^\infty K_0(2\sqrt{x}) \exp\left(-\frac{\rho L^2 |s_{\hat{k}}|^2}{2} x\right) dx. \quad (54)$$

Resort to (35), we can rewrite (54) as

$$\bar{P}_b = \frac{\exp\left(\frac{1}{2\alpha}\right)}{2\sqrt{\alpha}} \Gamma(v+1) \Gamma(1-v) W_{-\frac{1}{2}, v} \left(\frac{1}{\alpha} \right). \quad (55)$$

After some simplifications, we complete the proof.

Note that (53) contains Whittaker function, it is not closed-form expression, which limits the contribution of this work. To tackle this issue, we resort to the following method.

2) **Method 2:** To obtain the closed-form expression of UPEP, we can derive the UPEP under $\hat{m} \neq m$ scenario as

$$\begin{aligned} \bar{P}_b &= \frac{1}{2} \int_0^\infty \exp\left(-\frac{\rho L^2 |s_{\hat{k}}|^2}{2} x\right) f(x) dx \\ &= \sum_{v=0}^\infty \frac{x^v}{(v!)^2} \int_0^\infty \exp\left(-\frac{\rho L^2 |s_{\hat{k}}|^2}{2} x\right) \\ &\quad \times \left[-\frac{1}{2} \ln(x) + \psi(v+1) \right] dx \\ &= -\frac{1}{2} \sum_{v=0}^\infty \frac{1}{(v!)^2} \underbrace{\int_0^\infty x^v \ln(x) \exp\left(-\frac{\rho L^2 |s_{\hat{k}}|^2}{2} x\right) dx}_{C_1} \\ &\quad + \sum_{v=0}^\infty \frac{\psi(v+1)}{(v!)^2} \underbrace{\int_0^\infty x^v \exp\left(-\frac{\rho L^2 |s_{\hat{k}}|^2}{2} x\right) dx}_{C_2}, \end{aligned} \quad (56)$$

where $f(x) = 2 \sum_{v=0}^\infty \frac{x^v}{(v!)^2} \left[-\frac{1}{2} \ln(x) + \psi(v+1) \right]$ can be obtained via the (30) and (41).

By applying the (81), the C_1 in (56) can be obtained as

$$C_1 = v! \left(\frac{2}{\rho L^2 |s_{\hat{k}}|^2} \right)^{v+1} \left[\psi(v+1) - \ln\left(\frac{\rho L^2 |s_{\hat{k}}|^2}{2} \right) \right]. \quad (57)$$

According to [33], we get

$$\int_0^\infty x^p \exp(-\beta x^q) dx = \frac{\Gamma(\gamma)}{q\beta^\gamma}, \quad (58)$$

where $\gamma = \frac{p+1}{q}$. By combining (58) and (56), then (56) can be re-represented as

$$C_2 = v! \left(\frac{2}{\rho L^2 |s_{\hat{k}}|^2} \right)^{v+1}. \quad (59)$$

Replacing (57) and (59) into (56), we can obtain the UPEP as

$$\begin{aligned} \bar{P}_b &= -\frac{1}{2} \sum_{v=0}^\infty \frac{1}{v!} \left(\frac{2}{\rho L^2 |s_{\hat{k}}|^2} \right)^{v+1} \left[\psi(v+1) - \ln\left(\frac{\rho L^2 |s_{\hat{k}}|^2}{2} \right) \right] \\ &\quad + \sum_{v=0}^\infty \frac{\psi(v+1)}{v!} \left(\frac{2}{\rho L^2 |s_{\hat{k}}|^2} \right)^{v+1} \\ &= \frac{1}{2} \sum_{v=0}^\infty \frac{1}{v!} \left(\frac{2}{\rho L^2 |s_{\hat{k}}|^2} \right)^{v+1} \left[\ln\left(\frac{\rho L^2 |s_{\hat{k}}|^2}{2} \right) + \psi(v+1) \right]. \end{aligned} \quad (60)$$

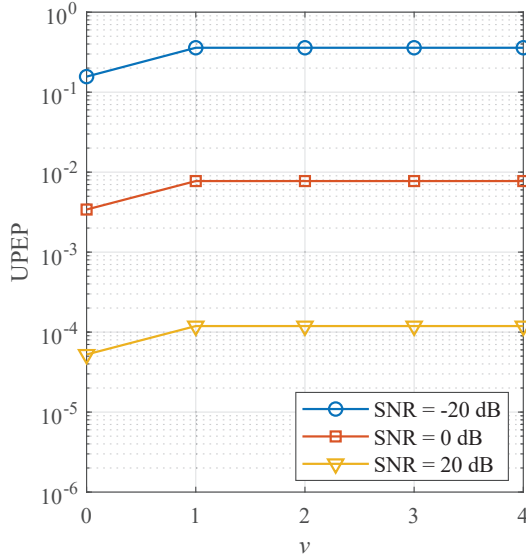


Fig. 2. Coverage analysis.

C. Asymptotic UPEP

In this subsection, we investigate the asymptotic expression of UPEP from (45) and (60). It can be observed that the expressions (45) and (60) are summed by an infinite number of terms, which makes our computation very difficult. To cope with this challenge, we select the term that plays a dominant role in UPEP as an asymptotic expression to characterize UPEP. As shown in Fig. 2, we describe the relationship between the number of summation terms of (45) and (60) and the value of UPEP. It can be observed that as v increases, UPEP achieves convergence at $v = 1$. In particular, Fig. 2 shows that there is a slight gap between the UPEP obtained when $v = 0$ and $v = 1$ due to the fact that in (45) the first term is obtained at $v = 1$, while in (60) the first term is obtained from $v = 0$. Besides, Fig. 2 shows that increasing the SNR leads to better UPEP performance. As such, the first term of (45) and (60) can guarantee to represent the whole values of the (45) and (60), which validates that the correctness of the operation in (61) and (62), respectively. As a result, we can obtain the approximating UPEP as follows:

1) $\hat{m} = m$: Recalling Fig. 6, we observe that most of the information is concentrated in the first item. Moreover, we aim to obtain the trend of ABEP changing with SNR. As such, the main term of the (45) can be obtained as

$$\bar{P}_a = \frac{1}{\rho L^2 \bar{\eta}} \left[\ln \left(\frac{\rho L^2 \bar{\eta}}{4} \right) - \psi \left(\frac{3}{2} \right) + 1 + 2\psi(1) \right]. \quad (61)$$

2) $\hat{m} \neq m$: Combing (60), the asymptotic PEP in this case can be evaluated as

$$\bar{P}_a = \frac{1}{\rho L^2 |s_{\hat{k}}|^2} \left[\ln \left(\frac{\rho L^2 |s_{\hat{k}}|^2}{2} \right) + \psi(1) \right]. \quad (62)$$

D. Diversity Gain

In this subsection, we derive the diversity order \mathcal{D} of the proposed RIS-DSSM scheme based on the asymptotic UPEP expression. It is worth noting that \mathcal{D} is the high-SNR slope of the PEP determined from a figure plotted in a log-log scale. In

the following, the $\hat{m} = m$ and $\hat{m} \neq m$ cases are respectively derived as follows:

1) $\hat{m} = m$: In this case, the \mathcal{D} can be evaluated as

$$\begin{aligned} \mathcal{D} &= \lim_{\rho \rightarrow \infty} -\frac{\log_2(\bar{P}_a)}{\log_2 \rho} = \lim_{\rho \rightarrow \infty} \frac{\log_2 \left(\frac{\rho L^2 \bar{\eta}}{\ln \left(\frac{\rho L^2 \bar{\eta}}{4} \right)} \right)}{\log_2 \rho} \\ &= \lim_{\rho \rightarrow \infty} \frac{\log_2(\rho L^2 \bar{\eta})}{\log_2 \rho} = 1. \end{aligned} \quad (63)$$

2) $\hat{m} \neq m$: In this case, the \mathcal{D} can be calculated as

$$\begin{aligned} \mathcal{D} &= \lim_{\rho \rightarrow \infty} -\frac{\log_2(\bar{P}_a)}{\log_2 \rho} = \lim_{\rho \rightarrow \infty} \frac{\log_2 \left(\frac{\rho L^2 |s_{\hat{k}}|^2}{\ln \left(\frac{\rho L^2 |s_{\hat{k}}|^2}{2} \right)} \right)}{\log_2 \rho} \\ &= \lim_{\rho \rightarrow \infty} \frac{\log_2(\rho L^2 |s_{\hat{k}}|^2)}{\log_2 \rho} = 1. \end{aligned} \quad (64)$$

E. ABEP

In this subsection, we evaluate the error performance of the RIS-DSSM system, where $\log_2(NMK)$ bits are utilized for transmission. Note that the union upper bound of ABEP is given by

$$\text{ABEP} \leq \sum_{n=1}^N \sum_{m=1}^M \sum_{k=1}^K \sum_{\hat{n}=1}^N \sum_{\hat{m}=1}^M \sum_{\hat{k}=1}^K \frac{N([n, m, k] \rightarrow [\hat{n}, \hat{m}, \hat{k}]) \bar{P}_b}{NMK \log_2(NMK)}, \quad (65)$$

where $N([n, m, k] \rightarrow [\hat{n}, \hat{m}, \hat{k}])$ represents the number of error bits between the original bits $[n, m, k]$ and the decision bits $[\hat{n}, \hat{m}, \hat{k}]$.

IV. SIMULATION AND ANALYTICAL RESULTS

In this section, simulation and analytical results are presented to evaluate the RIS-DSSM performance for mmWave transmissions. At first, the detection overhead and ABEP of the optimal and suboptimal detectors are evaluated, where the N_t and N_r are set as 32 for the simulations [14]. Then, link-level simulations verify the correctness of the analytical derivations of the proposed RIS-DSSM scheme. Afterward, we evaluate the ABEP performance versus different parameters. Finally, the proposed RIS-DSSM scheme is compared with the conventional SSM in terms of reliability. All simulation results are randomly generated 1×10^7 channel realizations and then averaged. The central frequency of the considered carrier in this paper is 28 GHz [34].

A. Comparing the Complexity of Suboptimal and Optimal Detectors

In this subsection, we present the computational complexity of the detectors at the Rx for the RIS-DSSM schemes, which can be obtained by finding the number of real additions and real multiplications. Noting that each complex multiplication requires 4 real multiplications and 2 real summations, while the square of the absolute value of the complex number requires 2 real multiplications and 1 real addition. In the subsequent analysis, we compare the complexity of the suboptimal and optimal detectors for the RIS-DSSM scheme.

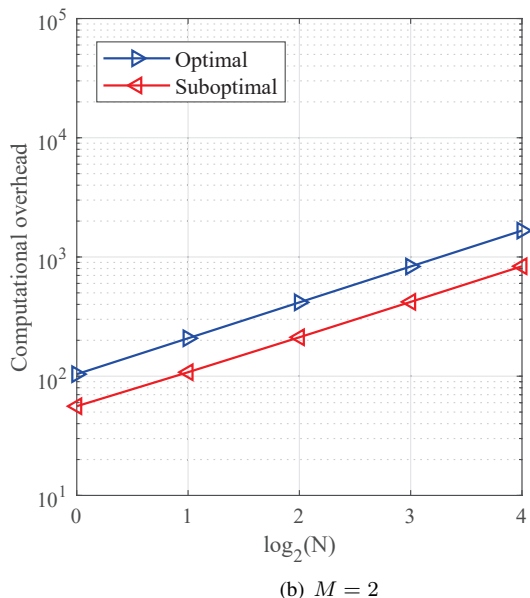
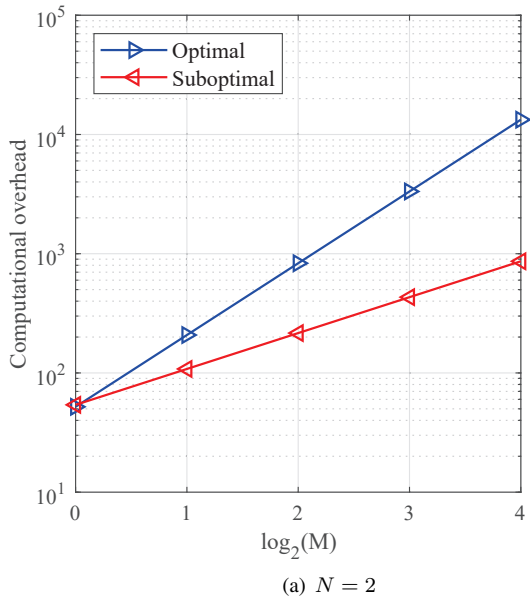


Fig. 3. Comparison analysis of computational overhead.

To simplify the analysis, we apply (9) to optimal and suboptimal detectors. Recalling that suboptimal detection is composed of (19) and (22). In terms of (19), the real complexity of the required multiplications and summations are $2M$ and M , respectively. For the suboptimal detector, the (22) can be described as

$$[\hat{n}, \hat{m}, \hat{k}] = \arg \min_{\substack{n \in \{1, \dots, N\} \\ m \in \{1, \dots, M\} \\ k \in \{1, \dots, K\}}} \left| \mathbf{y}_r(m) - \sqrt{P_s} L h_m g_n s_k \right|^2, \quad (66)$$

where $h_m g_n s_k$ can be calculated by the multiplication of three complex numbers with 8 real multiplications and 4 real summations. Multiplication of $\sqrt{P_s} L$ accompanies 3 real multiplications, while subtracting $\sqrt{P_s} L h_m g_n s_k$ from $\mathbf{y}_r(m)$ requires 2 real summations. The square of the absolute value of the calculated complex value is also taken into account,

as well as the repetition of this process for each symbol and scatterer in the Tx-RIS and RIS-Rx channels, respectively. As such, the calculations of (19) and (66) require $13MNK + 2M$ multiplications and $7MNK + M$ summations. On the other hand, for the optimal detector, the (18) based on (9) can be obtained as

$$[\hat{n}, \hat{m}, \hat{k}] = \arg \min_{\substack{n \in \{1, \dots, N\} \\ m \in \{1, \dots, M\} \\ k \in \{1, \dots, K\}}} \sum_{m=1}^M \left| \mathbf{y}_r(m) - \sqrt{P_s} L h_m g_n s_k \right|^2. \quad (67)$$

It is worth noting that the complexity of the optimal detection algorithm is about M times that of the suboptimal algorithm. The complexity of the optimal detection can be expressed as $13M^2NK$ multiplications and $7M^2NK$ summations.

The summation and multiplication operations have similar forms, without loss of generality, we only plot the complexity overhead of the multiplication operation in Fig. 3. It is worth mentioning that unless otherwise stated, the parameters are set to $M = 2, N = 2, K = 2$, and $L = 100$. As M increases, the gap between optimal detection and suboptimal detection gradually widens shown in Fig. 3(a), while in Fig. 3(b), as N increases, the gap between optimal detection and suboptimal detection remains stable. This phenomenon can be explained by (66) and (67), respectively.

B. ABEP Comparison of Suboptimal and Optimal Detectors

In Fig. 4, we perform a comparative analysis of the ABEP performance of the optimal and suboptimal detection algorithms. As expected, optimal detection exhibits better performance than suboptimal detection. Unless otherwise stated, parameters are set to $M = 2, N = 2, K = 2$, and $L = 100$. To be specific, when $\text{ABEP} = 10^{-3}$, the SNR required for the suboptimal algorithm in Fig. 4(a) and Fig. 4(b) is about 5 dB and 7 dB more than that of the optimal algorithm, respectively. It is worth mentioning that the inferior performance of the suboptimal algorithm compared to the optimal algorithm is the cost of the detection complexity.

C. Validation of Analytical Derivations

In Fig. 5(a), we illustrate the exactness of the union upper bound of ABEP for the proposed RIS-DSSM scheme, where the parameters are set as with $M = 2, N = 2, M = 2, N = 4$, and $M = 4, N = 4$. Without loss of generality, the BPSK signal for the symbol domain is employed. From Fig. 5(a), we see that the analytical and simulation results match closely at moderate to high SNRs, which illustrates the exactness of the analytical ABEP expressions of (37) and (53). Moreover, the ABEP performance of RIS-DSSM deteriorates as the number of modulated scatterers increases. This is because involving more scatterers in modulation increases the number of constellation points available in the spatial domain, which reduces decoding success probability. In an environment with abundant scatterers, we can select scatterers with better channel gain to participate in the modulation, while ignoring scatterers with poorer gain. In this manner, when more scatterers are participating in the modulation, the spectral efficiency increases.

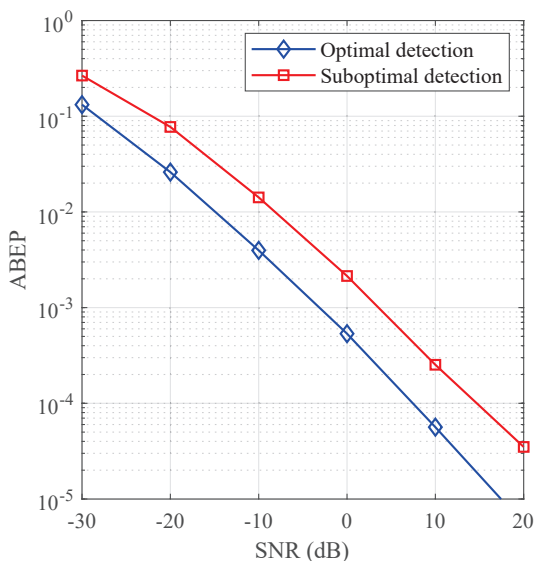
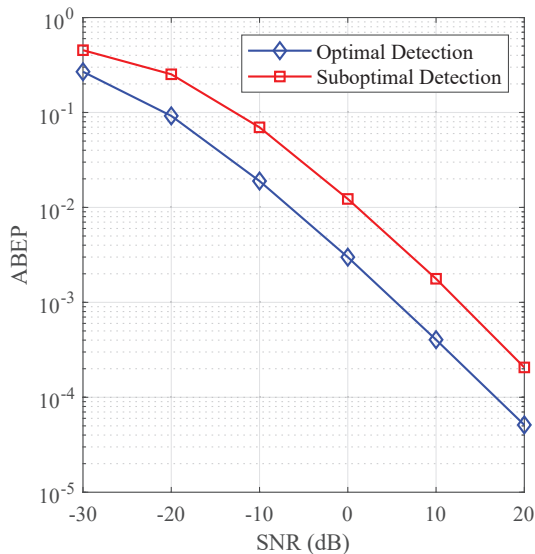
(a) $N = 2$ (b) $M = 2$

Fig. 4. Comparison analysis of ABEP.

In Fig. 5(b), we validate the upper bound expressions (38) of UPEP the versus the exact integral expression (37) of UPEP under different modulation orders with respect with the spatial domain. It can be seen from Fig. 5(b) that the ABEP based on upper bound expressions (38) are closely matched by the ABEP based on exact UPEP integral expression. This is because we divide the spatial domain into two parts, beam correct decoding and incorrect decoding, and the derived upper bound is in beam correct demodulation. The probability of beam incorrect decoding becomes larger as the modulation order in the spatial domain rises, and the percentage of this part of beam correct demodulation decreases. Hence, as the spatial domain modulation order rises, the difference between the obtained upper bound and the exact integral expression of ABEP is relatively small.

In Fig. 6, we validate the accuracy of the derived closed-

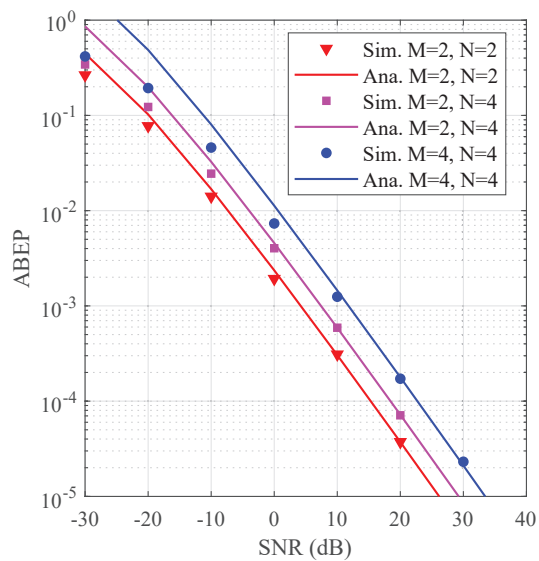
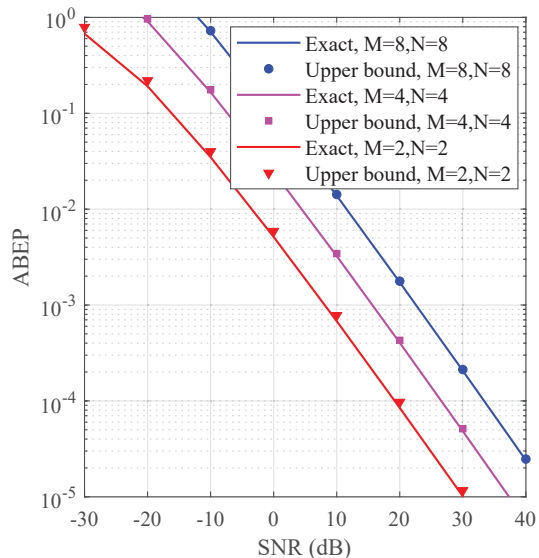
(a) $L = 100$ (b) $L = 64$

Fig. 5. Verification of analytical derivation results.

form asymptotic expression with the exact integral expression of ABEP, where closed-form expression is consist of (61) and (62) and integral ABEP is consist of (37) and (53). The parameters are set as $M = 2, N = 2, K = 2$, and $L = 64$. It can be seen from Fig. 6 that, in the region of -20 dB to 30 dB, the closed-form asymptotic expression and the integral expression are in good agreement. However, in the enlarged subfigure, we can find slightly lower values for the closed-form asymptotic expression than the exact integral expression. This is because we take the first term of (61) and (62) to approximate the whole expression, which is highlighted in Fig. 2. To improve the accuracy, we can increase the number of selected terms of the closed-form expression.

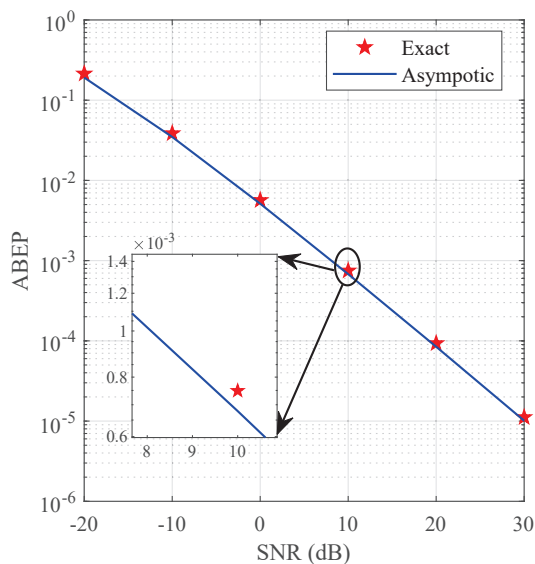


Fig. 6. Verification of analytical derivation results.

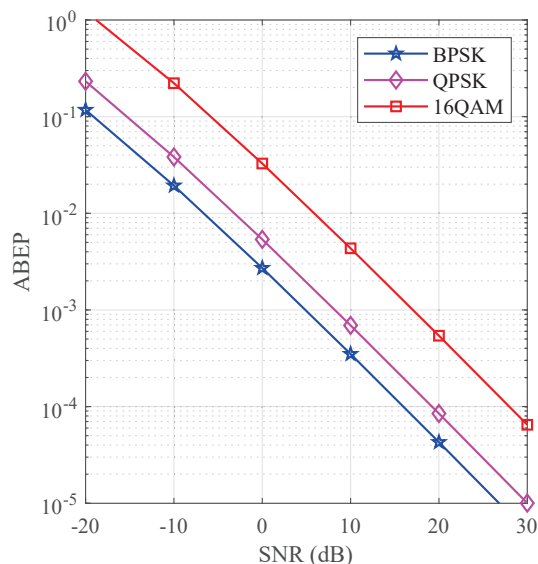
D. Performance Analysis of ABEP with Different Parameters

Fig. 7(a) shows a comparison of the ABEPs for the RIS-DSSM system using BPSK, QPSK, and 16QAM signal constellations at data rates of 3 bit per channel use (bpcu), 4 bpcu, and 6 bpcu, respectively, where gray mapping is applied to all symbol modulations. It can be observed from Fig. 7(a) that these systems vary in performance. To be specific, when ABEP is 10^{-4} , systems with QPSK and 16QAM require approximately 3 dB and 9 dB higher SNRs than the BPSK system. This is because, in the normalized symbol constellation diagram, the increasing modulation order leads to a denser distribution of constellation points, resulting in a smaller Euclidean distance between adjacent constellation points.

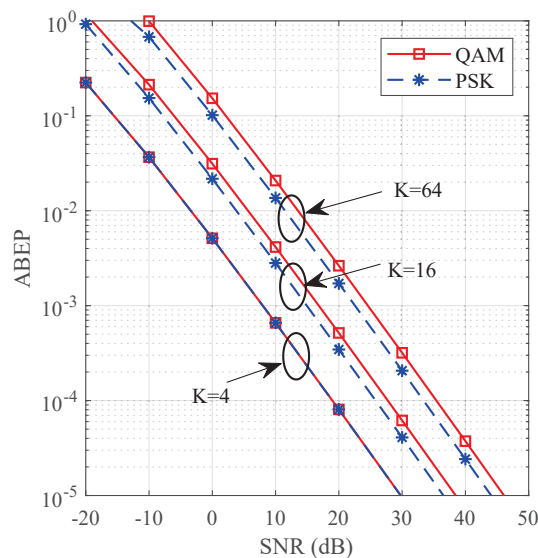
Fig. 7(b) depicts the plot of the ABEP of the RIS-DSSM system versus the SNRs with K -ary PSK and QAM applied in the symbol domain. It can be observed from Fig. 7(b) that for the considered parameters with 4QAM and QPSK can obtain the same performance since the constellation diagrams of 4QAM and QPSK are consistent. Further, it can also be observed that at the same error rate, the higher the modulation order, the greater the required transmit SNR. From this observation, we find that the system with 16PSK has a better performance than that of 16QAM. Meanwhile, the system with 64PSK performs better than that of 64QAM. This is because (52)-based ABEP is only related to the amplitude of $s_{\hat{k}}$, whereas in 16-order and 64-order modulation systems, the average amplitude of the PSK signal is large than that of the QAM signal.

E. Comparison to the Conventional SSM

Fig. 8 depicts the ABEP values of the SSM and RIS-DSSM schemes under different SNRs, where the number of RIS elements in the RIS-DSSM scheme is respectively taken as 1, 4, 16, and 64. The simulation parameters of the RIS-DSSM scheme are configured as $M = 2, N = 2$, and $K = 2$. In contrast, the number of scatterers and the symbol field in the SSM scheme are set to 4 and BPSK, respectively. As expected,



(a) $M = 2, N = 2, L = 100$



(b) $M = 2, N = 2, L = 100$

Fig. 7. ABEP under different parameters.

the Monte Carlo simulation results are similar to the ABEP obtained via the closed-form expressions in (45) and (60). It can be seen that the performance of SSM dominates at $L = 1$, while RIS-DSSM outperforms SSM at higher values of L . The reason for this phenomenon is that when $L = 1$, RIS cannot form a specific beam directed at the scatterer, which leads to a larger value of ABEP. In contrast, when L is larger, the beam directed to the scatterer is more refined and stronger in energy, thus obtaining a better system performance. It is also interesting to analyze the minimum L for which the RIS-DSSM scheme outperforms the SSM scheme. In this regard, when the receiving beam is demodulated correctly or not, we obtain the following two equations to determine the minimum

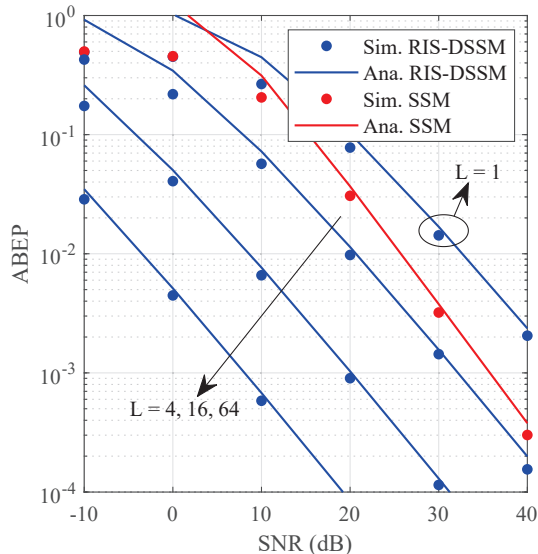


Fig. 8. Comparison with traditional SSM scheme.

L .

$$L^2 - \frac{13}{24} \ln \left(\frac{\rho L^2 \bar{\eta}}{4} \right) + \frac{13}{24} \left[\psi \left(\frac{3}{2} \right) - 1 - 2\psi(1) \right] \leq 0, \quad (68)$$

$$L^2 - \ln \left(\frac{\rho L^2 |s_{\hat{k}}|^2}{2} \right) - \psi(1) \leq 0. \quad (69)$$

The detailed derivation is presented in Appendix F. However, due to the complexity of the formulas, it is not possible to obtain the closed-form solution directly. Nevertheless, we observe that the parameter affecting the performance of the two systems is not only related to the number of reflecting elements L , but also to the SNR ρ .

V. CONCLUSIONS AND FUTURE WORK

In this paper, we conducted a study on the ABEP of a RIS-assisted DSSM system in mmWave MIMO systems. To decrease detection complexity, a suboptimal detection algorithm was presented and compared with the ML-based optimal detection algorithm. Using the suboptimal detector, the exact integral ABEP and closed-form ABEP expressions were respectively obtained via the two different methods. Moreover, the upper bound and asymptotic expressions of ABEP on the RIS-DSSM scheme are provided. Monte Carlo simulations were used to validate the correctness of the analytical derivations. Our results showed that the analytical upper bound and asymptotic ABEP keep close agreement with the exact integral results. Furthermore, as the number of RIS elements increases, the RIS-DSSM scheme outperforms conventional SSM scheme in terms of reliability. For future work, the impact of channel estimation errors on the performance of RIS-DSSM systems can be explored. In addition, evaluating the system performance from other metrics, such as ergodic capacity, and system throughput, is still an interesting and open research topic.

APPENDIX A PROOF OF LEMMA 1

For the large number of the transmit antennas equipped at the Tx, the inner product of the two steering vectors can be written as

$$\begin{aligned} \mathbf{a}_t^H(\theta_n^t) \mathbf{a}_t(\theta_{n'}^t) &= \frac{1 - \exp(j2\pi(\theta_{n'}^t - \theta_n^t)N_t)}{N_t - N_t \exp(j2\pi(\theta_{n'}^t - \theta_n^t))} \\ &= \frac{\sin(\pi(\theta_{n'}^t - \theta_n^t)N_t)}{N_t \sin(\pi(\theta_{n'}^t - \theta_n^t))} \exp(j\pi(\theta_{n'}^t - \theta_n^t)(N_t - 1)), \end{aligned} \quad (70)$$

where n and n' indicate that two transmit beams are directed at two different scatterers. Afterward, we take the absolute value of (70) and represent the operation as

$$|\mathbf{a}_t^H(\theta_n^t) \mathbf{a}_t(\theta_{n'}^t)| = \frac{1}{N_t} \left| \frac{\sin(\pi(\theta_{n'}^t - \theta_n^t)N_t)}{\sin(\pi(\theta_{n'}^t - \theta_n^t))} \right|. \quad (71)$$

Without loss of generality, we consider that the scatterers involved in the modulation are all between the Tx and Rx channels, satisfying $(\theta_{n'}^t - \theta_n^t) \in [-\frac{\pi}{2}, \frac{\pi}{2}]$. Hence, we have

$$\left| \frac{\sin(\pi(\theta_{n'}^t - \theta_n^t)N_t)}{\sin(\pi(\theta_{n'}^t - \theta_n^t))} \right| \neq 0. \quad (72)$$

When $N_t \rightarrow \infty$, we have $|\mathbf{a}_t^H(\theta_n^t) \mathbf{a}_t(\theta_{n'}^t)| = 0$. It is worth noting that we can obtain the corresponding proof for the receive array. Here, the proof of **Lemma 1** is completed.

APPENDIX B PROOF OF LEMMA 2

It is clear to observe that the variables g and s are coupled together. To address this issue, we decompose η into real part and the imaginary part. After that, we discuss both cases $\hat{n} = n$ and $\hat{n} \neq n$ separately.

1) In $\hat{n} = n$ case, we define $\eta = |g_n s_k - g_{\hat{n}} s_{\hat{k}}|^2$, then the average $\bar{\eta}$ can be derived as

$$\begin{aligned} \bar{\eta} &= E[|\zeta|^2] + E[|\xi|^2] \\ &= E \left[|\Re(g_n s_k) - \Re(g_{\hat{n}} s_{\hat{k}})|^2 \right] \\ &\quad + E \left[|\Im(g_n s_k) - \Im(g_{\hat{n}} s_{\hat{k}})|^2 \right] \\ &= E \left[|\Re(g_n) (s_k - s_{\hat{k}})|^2 \right] + E \left[|\Im(g_n) (s_k - s_{\hat{k}})|^2 \right]. \end{aligned} \quad (73)$$

For variable β , x_{\Re} and x_{\Im} can be viewed as constants. Consequently, we have

$$\begin{aligned} \bar{\eta} &= E \left[|\Re(g_n)|^2 |s_k - s_{\hat{k}}|^2 \right] + E \left[|\Im(g_n)|^2 |s_k - s_{\hat{k}}|^2 \right] \\ &= E [g_n^2] |s_k - s_{\hat{k}}|^2. \end{aligned} \quad (74)$$

Since g_n follows $\mathcal{CN}(0, 1)$, the $E[g_n^2] = \mu_{g_n}^2 + \sigma_{g_n}^2$. At this time, we can obtain $\bar{\eta} = |s_k - s_{\hat{k}}|^2$.

2) In $\hat{n} \neq n$ case, the value of $\bar{\eta}$ can be we derived as

$$\begin{aligned}
\bar{\eta} &= E[|\zeta|^2] + E[|\xi|^2] \\
&= E \left[|\Re(g_n s_k) - \Re(g_{\hat{n}} s_{\hat{k}})|^2 \right] \\
&\quad + E \left[|\Im(g_n s_k) - \Im(g_{\hat{n}} s_{\hat{k}})|^2 \right] \\
&= E \left[|\Re(g_n)|^2 |s_k|^2 + E \left[|\Re(g_{\hat{n}})|^2 \right] |s_{\hat{k}}|^2 \right] \\
&\quad + E \left[|\Im(g_n)|^2 |s_k|^2 + E \left[|\Im(g_{\hat{n}})|^2 \right] |x_{\hat{k}}|^2 \right] \quad (75) \\
&= \left(E \left[|\Re(g_n)|^2 \right] + E \left[|\Im(g_n)|^2 \right] \right) |s_k|^2 \\
&\quad + \left(E \left[|\Re(g_{\hat{n}})|^2 \right] + E \left[|\Im(g_{\hat{n}})|^2 \right] \right) |s_{\hat{k}}|^2 \\
&= E \left[g_n^2 \right] |s_k|^2 + E \left[g_{\hat{n}}^2 \right] |s_{\hat{k}}|^2 \\
&= |s_k|^2 + |s_{\hat{k}}|^2.
\end{aligned}$$

Herein, the proof of **Lemma 2** is completed.

APPENDIX C PROOF OF THEOREM 1

Without loss of generality, let us define $x = |g_n h_m|^2$, where $x_1 = |g_n|^2$ and $x_2 = |h_m|^2$. Since both x_1 and x_2 follow independent and identically distributed $\mathcal{CN}(0, 1)$, the cumulative distribution function (CDF) of x can be derived as follows:

$$\begin{aligned}
F_X(x) &= P_r(X < x) = P_r(x_1 x_2 \leq x) \\
&= \int_0^\infty P_r(x_1 \leq \frac{x}{x_2} | x_2) f(x_2) dx_2 \quad (76) \\
&= \int_0^\infty F\left(\frac{x}{x_2}\right) f(x_2) dx_2.
\end{aligned}$$

Recall that $g_n \sim \mathcal{CN}(0, 1)$ and $h_m \sim \mathcal{CN}(0, 1)$. After some mathematical operations, the PDF and CDF can be respectively given as

$$F_{X_i}(x) = 1 - \exp(-x), \quad f_{X_i}(x) = \exp(-x), \quad i \in \{1, 2\}. \quad (77)$$

By inserting (77) into (76), we can further write (76) as

$$\begin{aligned}
F_X(x) &= 1 - \int_0^\infty \exp\left(-\frac{x}{x_2}\right) \exp(-x_2) dx_2 \quad (78) \\
&= 1 - 2\sqrt{x} K_1(2\sqrt{x}).
\end{aligned}$$

Based on (78), we can get $f(x) = \frac{dF_X(x)}{dx}$. At this time, the proof of **Theorem 1** is completed.

APPENDIX D PROOF OF THEOREM 2

By substituting $Q(x) = \frac{1}{\pi} \int_0^{\frac{\pi}{2}} \exp\left(-\frac{x^2}{2 \sin^2 \theta}\right) d\theta$ into (42), the A_1 can be written as

$$A_1 = \frac{1}{\pi} \int_0^\infty \int_0^{\frac{\pi}{2}} x^v \ln(x) \exp\left(-\frac{\rho L^2 \bar{\eta} x}{4 \sin^2 \theta}\right) d\theta dx. \quad (79)$$

Exchange the order of integration of variables θ and x , A_1 can be further expressed as

$$A_1 = \frac{1}{\pi} \int_0^{\frac{\pi}{2}} \int_0^\infty x^v \ln(x) \exp\left(-\frac{\rho L^2 \bar{\eta} x}{4 \sin^2 \theta}\right) dx d\theta. \quad (80)$$

According to [33], we have

$$\int_0^\infty x^v \ln(x) \exp\left(-\frac{ax}{b}\right) dx = \frac{b^{v+1}}{a^{v+1}} v! \left[\psi(v+1) - \ln\left(\frac{a}{b}\right) \right]. \quad (81)$$

Substituting (81) into (80), the A_1 can be represented as

$$\begin{aligned}
A_1 &= \frac{1}{\pi} \int_0^{\frac{\pi}{2}} \int_0^\infty x^v \ln(x) \exp\left(-\frac{\rho L^2 \bar{\eta} x}{4 \sin^2 \theta}\right) dx d\theta \\
&= \frac{1}{\pi} \int_0^{\frac{\pi}{2}} \left(\frac{4 \sin^2 \theta}{\rho L^2 \bar{\eta}}\right)^{v+1} v! \left[\psi(v+1) - \ln\left(\frac{\rho L^2 \bar{\eta}}{4 \sin^2 \theta}\right) \right] d\theta \\
&= \frac{v!}{\pi} \left(\frac{4}{\rho L^2 \bar{\eta}}\right)^{v+1} \int_0^{\frac{\pi}{2}} (\sin \theta)^{2v+2} \\
&\quad \times \left[\psi(v+1) + \ln\left(\frac{4}{\rho L^2 \bar{\eta}}\right) + 2 \ln(\sin \theta) \right] d\theta \\
&= \frac{v!}{\pi} \left(\frac{4}{\rho L^2 \bar{\eta}}\right)^{v+1} \left[\psi(v+1) + \ln\left(\frac{4}{\rho L^2 \bar{\eta}}\right) \right] \\
&\quad \times \underbrace{\int_0^{\frac{\pi}{2}} (\sin \theta)^{2v+2} d\theta}_{B_1} \\
&\quad + 2 \frac{v!}{\pi} \left(\frac{4}{\rho L^2 \bar{\eta}}\right)^{v+1} \underbrace{\int_0^{\frac{\pi}{2}} (\sin \theta)^{2v+2} \ln(\sin \theta) d\theta}_{B_2}. \quad (82)
\end{aligned}$$

In order to obtain the result of the integral, we refer to [33] to deal with B_1 and B_2 as

$$B_1 = \int_0^{\frac{\pi}{2}} (\sin \theta)^{2v+2} d\theta = \frac{\pi (2v+1)!!}{2 (2v+2)!!}, \quad (83)$$

and

$$\begin{aligned}
B_2 &= \int_0^\infty \ln(\sin \theta) (\sin \theta)^{2v+2} d\theta \\
&= \frac{\pi (2v+1)!!}{2 (2v+2)!!} \left[\sum_{q=1}^{2v+2} \frac{(-1)^{q+1}}{q} - \ln 2 \right]. \quad (84)
\end{aligned}$$

To facilitate the subsequent operations, we apply the following equivalent transformation as [33]

$$\sum_{q=1}^{2v+2} \frac{(-1)^{q+1}}{q} = \ln 2 + \frac{1}{2} \left[\psi\left(v + \frac{3}{2}\right) - \psi(v+2) \right]. \quad (85)$$

Replacing (85) with (84), we can rewrite B_2 as

$$B_2 = \frac{\pi (2v+1)!!}{4 (2v+2)!!} \left[\psi\left(v + \frac{3}{2}\right) - \psi(v+2) \right]. \quad (86)$$

At this point, by substituting the derived (83) and (86) into the (82), A_1 can be evaluated as

$$\begin{aligned}
A_1 &= \frac{v!}{2} \left(\frac{4}{\rho L^2 \bar{\eta}}\right)^{v+1} \frac{(2v+1)!!}{(2v+2)!!} \\
&\quad \times \left[\psi(v+1) - \psi(v+2) + \ln\left(\frac{4}{\rho L^2 \bar{\eta}}\right) + \psi\left(v + \frac{3}{2}\right) \right]. \quad (87)
\end{aligned}$$

To simplify for (87), we obtain from [33]

$$\psi(v+1) - \psi(v+2) = -\frac{1}{v+1}. \quad (88)$$

Finally, we insert (88) into (87), the proof **Theorem 2** is completed.

APPENDIX E
PROOF OF THEOREM 3

Substituting $Q(x) = \frac{1}{2}\text{erfc}\left(\frac{x}{\sqrt{2}}\right)$ into A_2 , it can be rewritten as

$$A_2 = \frac{1}{2} \int_0^\infty x^v \text{erfc}\left(\sqrt{\frac{\rho L^2 \bar{\eta} x}{4}}\right) dx. \quad (89)$$

Let us define $y = \sqrt{\frac{\rho L^2 \bar{\eta} x}{4}}$, A_2 can be rewritten as

$$A_2 = \left(\frac{4}{\rho L^2 \bar{\eta}}\right)^{v+1} \int_0^\infty y^{2v+1} \text{erfc}(y) dy. \quad (90)$$

According to [33], we have

$$\int_0^\infty x^{2q-1} \text{erfc}(x) dx = \frac{\Gamma(q + \frac{1}{2})}{2q\sqrt{\pi}}. \quad (91)$$

Next, we substitute this term into (90), the A_2 can be updated as

$$A_2 = \frac{1}{2} \left(\frac{4}{\rho L^2 \bar{\eta}}\right)^{v+1} \frac{\Gamma(v + \frac{3}{2})}{(v+1)\sqrt{\pi}}. \quad (92)$$

Resort to [33], we have

$$\Gamma\left(v + \frac{3}{2}\right) = \frac{(2v+1)!!\sqrt{\pi}}{2^{v+1}}, \quad (93)$$

$$2^{v+1} = \frac{(2v+2)!!}{(v+1)!}. \quad (94)$$

Substituting (93) and (94) into (92), the proof of **Theorem 3** is completed.

APPENDIX F
PROOF OF (68) AND (69)

To clarify the major parameters impacting the performance of ABEP, we resort to asymptotic expressions for our analysis. It is worth mentioning that we divide the received beams into two cases, correctly decoded and incorrectly decoded, for discussion.

Case 1: If the detected beam is demodulated correctly, i.e., $\hat{m} = m$, the asymptotic UPEP of the SSM can be expressed as [15]

$$\bar{P}_a^{\text{SSM}} = \frac{24}{13\rho\bar{\eta}}. \quad (95)$$

Recall that (61), the asymptotic UPEP of RIS-DSSM scheme is given by

$$\bar{P}_a^{\text{RIS-DSSM}} = \frac{1}{\rho L^2 \bar{\eta}} \left[\ln\left(\frac{\rho L^2 \bar{\eta}}{4}\right) - \psi\left(\frac{3}{2}\right) + 1 + 2\psi(1) \right]. \quad (96)$$

To obtain the minimal number of elements that RIS-DSSM better than SSM scheme, we let $\bar{P}_a^{\text{RIS-DSSM}} \leq \bar{P}_a^{\text{SSM}}$. After some manipulation operations, we have

$$L^2 - \frac{13}{24} \ln\left(\frac{\rho L^2 \bar{\eta}}{4}\right) + \frac{13}{24} \left[\psi\left(\frac{3}{2}\right) - 1 - 2\psi(1) \right] \leq 0. \quad (97)$$

By observation we find that the required variable L contains L^2 and $\frac{13}{24} \ln\left(\frac{\rho L^2 \bar{\eta}}{4}\right)$ in two items, and it is impossible to directly obtain the exact value of L . However, through (97) we find that the factors affecting the RIS-DSSM and SSM

schemes are not only related to the number of RIS cells but also to the SNR ρ .

Case 2: If the detected beam is demodulated incorrectly, i.e., $\hat{m} \neq m$, the CPEP of the SSM can be expressed as [14]

$$P_b = \frac{1}{2} \exp\left(-\frac{\rho|h_m|^2|s_k|^2}{2}\right). \quad (98)$$

Based on this, we derive the UPEP of SSM as

$$\bar{P}_b^{\text{SSM}} = \frac{1}{2} \int_0^\infty \exp\left(-\frac{\rho x|s_k|^2}{2}\right) \exp(-x) dx = \frac{1}{\rho|s_k|^2 + 2}. \quad (99)$$

In the high SNR region, the constant term in the denominator can be ignored. At this point, we have

$$\bar{P}_a^{\text{SSM}} = \lim_{\rho \rightarrow \infty} \frac{1}{\rho|s_k|^2 + 2} = \frac{1}{\rho|s_k|^2}. \quad (100)$$

Based on (62), the asymptotic UPEP can be given as

$$\bar{P}_a^{\text{RIS-DSSM}} = \frac{1}{\rho L^2 |s_k|^2} \left[\ln\left(\frac{\rho L^2 |s_k|^2}{2}\right) + \psi(1) \right]. \quad (101)$$

To obtain the minimal number of elements that RIS-DSSM better than SSM scheme, we let $\bar{P}_a^{\text{RIS-DSSM}} \leq \bar{P}_a^{\text{SSM}}$. Then, we have

$$L^2 - \ln\left(\frac{\rho L^2 |s_k|^2}{2}\right) - \psi(1) \leq 0. \quad (102)$$

Based on (102), we find that the variable L exists in L^2 and $\ln\left(\frac{\rho L^2 |s_k|^2}{2}\right)$ terms, which cannot be derived directly. However, we observed that the impact of the RIS-DSSM and SSM schemes is related to both the number of RIS elements L and ρ .

In summary, it is challenging to provide a precise quantitative assessment of the superiority of the RIS-DSSM system over the SSM system using analytical methods. Consequently, our paper primarily elucidates this distinction through simulation-based descriptions.

REFERENCES

- [1] L. Lu et al., "An overview of massive MIMO: Benefits and challenges," *IEEE J. Sel. Topics Signal Process.*, vol. 8, no. 5, pp. 742-58, Oct. 2014.
- [2] F. Wang, W. Chen, H. Tang, and Q. Wu, "Joint optimization of user association, subchannel allocation, and power allocation in multi-cell multi-association OFDMA heterogeneous networks," *IEEE Trans. Commun.*, vol. 65, no. 6, pp. 2672-2684, Jun. 2017.
- [3] C. Pan et al., "Reconfigurable intelligent surfaces for 6G systems: Principles, applications, and research directions," *IEEE Commun. Mag.*, vol. 59, no. 6, pp. 14-20, Jun. 2021.
- [4] Z. Li et al., "Towards transmissive RIS transceiver enabled uplink communication systems: Design and optimization," *IEEE Int. Things J.*, early access, doi: 10.1109/JIOT.2023.3312776.
- [5] Z. Li, W. Chen, Q. Wu, K. Wang, and J. Li, "Joint beamforming design and power splitting optimization in IRS-assisted SWIPT NOMA networks," *IEEE Trans. Wireless Commun.*, vol. 21, no. 3, pp. 2019-2033, Mar. 2022.
- [6] X. Bai et al., "High-efficiency transmissive programmable metasurface for multimode OAM generation," *Adv. Opt. Mater.*, vol. 8, no. 17, 2020, Art. no. 2000570.
- [7] E. Basar, M. Di Renzo, J. De Rosny, M. Debbah, M. -S. Alouini, and R. Zhang, "Wireless communications through reconfigurable intelligent surfaces," *IEEE Access*, vol. 7, pp. 116753-116773, Aug. 2019.
- [8] Z. Yigit, E. Basar, and I. Altunbas, "Low complexity adaptation for reconfigurable intelligent surface-based MIMO systems," *IEEE Commun. Lett.*, vol. 24, no. 12, pp. 2946-2950, Dec. 2020.

- [9] J. Wang, S. Gong, Q. Wu, and S. Ma, "RIS-aided MIMO systems with hardware impairments: Robust beamforming design and analysis," *IEEE Trans. Wireless Commun.*, early access, doi: 10.1109/TWC.2023.3246990.
- [10] R. Mesleh et al., "Spatial modulation," *IEEE Trans. Veh. Technol.*, vol. 57, no. 4, pp. 2228-2241, Jul. 2008.
- [11] X. Zhu, L. Yuan, Q. Li, Q. Li, L. Jin, and J. Zhang, "On the performance of 3-D spatial modulation over measured indoor channels," *IEEE Trans. Veh. Technol.*, vol. 71, no. 2, pp. 2110-2115, Feb. 2022.
- [12] J. Jeganathan, A. Ghrayeb, L. Szczecinski, and A. Ceron, "Space shift keying modulation for MIMO channels," *IEEE Trans. Wireless Commun.*, vol. 8, no. 7, pp. 3692-3703, Jul. 2009.
- [13] R. Mesleh, S. S. Ikki, and H. M. Aggoune, "Quadrature spatial modulation," *IEEE Trans. Veh. Technol.*, vol. 64, no. 6, pp. 2738-2742, Jun. 2015.
- [14] Y. Ding, K. J. Kim, T. Koike-Akino, M. Pajovic, P. Wang, and P. Orlik, "Spatial scattering modulation for uplink millimeter-wave systems," *IEEE Commun. Lett.*, vol. 21, no. 7, pp. 1493-1496, Jul. 2017.
- [15] X. Zhu, W. Chen, Z. Li, Q. Wu, and J. Li, "Quadrature spatial scattering modulation for mmWave transmission," *IEEE Commun. Lett.*, vol. 27, no. 5, pp. 1462-1466, May 2023.
- [16] E. Basar, "Reconfigurable intelligent surface-based index modulation: A new beyond MIMO paradigm for 6G," *IEEE Trans. Commun.*, vol. 68, no. 5, pp. 3187-3196, May 2020.
- [17] T. Ma, Y. Xiao, X. Lei, P. Yang, X. Lei, and O. A. Dobre, "Large intelligent surface assisted wireless communications with spatial modulation and antenna selection," *IEEE J. Sel. Areas Commun.*, vol. 38, no. 11, pp. 2562-2574, Nov. 2020.
- [18] S. Luo et al., "Spatial modulation for RIS-assisted uplink communication: Joint power allocation and passive beamforming design," *IEEE Trans. Commun.*, vol. 69, no. 10, pp. 7017-7031, Oct. 2021.
- [19] M. Wu, X. Lei, X. Zhou, Y. Xiao, X. Tang, and R. Q. Hu, "Reconfigurable intelligent surface assisted spatial modulation for symbiotic radio," *IEEE Trans. Veh. Technol.*, vol. 70, no. 12, pp. 12918-12931, Dec. 2021.
- [20] A. Bhowal, S. Aïssa, and R. S. Kshetrimayum, "RIS-assisted advanced spatial modulation techniques for ambient backscattering communications," *IEEE Trans. Green Commun. Networking*, vol. 5, no. 4, pp. 1684-1696, Dec. 2021.
- [21] S. Lin, F. Chen, M. Wen, Y. Feng, and M. Di Renzo, "Reconfigurable intelligent surface-aided quadrature reflection modulation for simultaneous passive beamforming and information transfer," *IEEE Trans. Wireless Commun.*, vol. 21, no. 3, pp. 1469-1481, Mar. 2022.
- [22] A. E. Canbilen, E. Basar, and S. S. Ikki, "Reconfigurable intelligent surface-assisted space shift keying," *IEEE Wireless Commun. Lett.*, vol. 9, no. 9, pp. 1495-1499, Sept. 2020.
- [23] X. Zhu, W. Chen, Q. Wu, and L. Wang, "Performance analysis of RIS-aided space shift keying with channel estimation errors," in *Proc. IEEE Int. Conf. Commun. China (ICCC)*, Aug. 2023, pp. 1-6.
- [24] X. Zhu et al., "Reconfigurable intelligent surface aided space shift keying with imperfect CSI," [Online] Available: <https://arxiv.org/abs/2309.03059>.
- [25] Q. Li, M. Wen, S. Wang, G. C. Alexandropoulos, and Y. -C. Wu, "Space shift keying with reconfigurable intelligent surfaces: Phase configuration designs and performance analysis," *IEEE Open J. Commun. Soc.*, vol. 2, pp. 322-333, Feb. 2021.
- [26] M. H. Dinan, N. S. Perovic, and M. F. Flanagan, "RIS-assisted receive quadrature space-shift keying: A new paradigm and performance analysis," *IEEE Trans. Commun.*, vol. 70, no. 10, pp. 6874-6889, Oct. 2022.
- [27] X. Zhu, et al. "RIS-assisted full-duplex space shift keying: System scheme and performance analysis," *IEEE Trans. Green Commun. Networking.*, early access, doi: 10.1109/TGCN.2023.3293913.
- [28] X. Zhu, W. Chen, Q. Wu, Z. Liu, and J. Li, "Performance of RIS-assisted full-duplex space shift keying with imperfect self-interference cancellation," *IEEE Wireless Commun. Lett.*, early access, doi: 10.1109/LWC.2023.3322939.
- [29] X. Zhu et al., "RIS-aided spatial scattering modulation for mmWave MIMO transmissions," *IEEE Trans. Commun.*, early access, doi: 10.1109/TCOMM.2023.3314636.
- [30] ———, "On the performance of RIS-aided spatial scattering modulation for mmWave transmission," [Online] Available: <https://arxiv.org/abs/2308.16804>.
- [31] X. Zhu, L. Yuan, K. J. Kim, Q. Li, and J. Zhang, "Reconfigurable intelligent surface-assisted spatial scattering modulation," *IEEE Commun. Lett.*, vol. 26, no. 1, pp. 192-196, Jan. 2022.
- [32] M. K. Simon, *Probability Distributions Involving Gaussian Random Variables: A Handbook for Engineers and Scientists*, Berlin, Germany: Springer, 2006.
- [33] A. Jeffrey, D. Zwillinger, I. Gradshteyn, and I. Ryzhik, *Table of Integrals, Series, and Products*, 7th ed. Boston, MA, USA: Academic, 2007.
- [34] Y. Liu, S. Zhang, F. Gao, J. Tang, and O. A. Dobre, "Cascaded channel estimation for RIS assisted mmWave MIMO transmissions," *IEEE Wireless Commun. Lett.*, vol. 10, no. 9, pp. 2065-2069, Sept. 2021.